

Simultaneous reflectance spectroscopy and thermal imaging on enzymatic reactions

First steps towards a new setup for monitoring enzymes in action

Bachelor's thesis

De Haagse Hogeschool

June 3, 2016

Author:
Sven Robert Iskander Meijer

Supervisor:
Dr. N. Bhattacharya

Coaches:
Dr. A.J. Lock
J.H.R. Lambers

Abstract

A setup is designed and constructed to perform specular reflectance spectroscopy on an enzymatic reaction, while simultaneously monitoring the heat produced by the reaction using a FLIR camera. The spectrum of ethanol was recorded using two MCT detectors and showed clear overlap with literature on ethanol's spectrum. However, for acquiring spectra faster, the setup was modified so the beam was coupled more efficiently onto the external detector. Together with a different way of calculating the spectrum, spectra were acquired in ≈ 6 minutes instead of > 15 minutes. Using this new method the spectrum of L-malate has been found, showing a peak in logarithmic reflectance at around 1100 cm^{-1} . Thermal imaging has been performed on the dehydration of L-malate, catalysed by fumarase. Only for 100 mM L-malate in water-like buffer features were detected that might indicate a temperature change due to dehydration, however it does not fit conventional ideas on endothermic reactions. For the oxidation of 3,3'-diaminobenzidine and L-tyrosine in the presence of hydrogen peroxide no features were detected. Even though the setup does allow for simultaneous measurements of spectroscopy and thermography, the experiments were carried out separately and independently.

Samenvatting

Een kwantumcascadelaser is gebruikt in een opstelling om directe reflectiespectroscopie uit te voeren op een enzymreactie, terwijl tegelijkertijd met een thermische camera van FLIR de door de reactie geproduceerde warmte wordt vastgelegd. Twee MCT detectoren zijn gebruikt om spectroscopische data vast te leggen. Bij wijze van test is spectroscopie uitgevoerd op ethanol. Het resulterende spectrum komt overeen met literatuurwaarden. Omdat het vastleggen van dit spectrum te lang duurde om nuttig te zijn in een enzymreactie is de opstelling verbeterd door een efficiëntere manier van focussen op de externe detector, samen met een nieuwe manier van berekenen. Op deze manier is de meettijd afgenomen van meer dan 15 minuten naar ongeveer 6 minuten. Met deze nieuwe methode is het spectrum van appelzuur vastgelegd met een piek rond 1100 cm^{-1} . Gescheiden van de spectroscopie is de temperatuursverandering vastgelegd voor de dehydratie appelzuur, gekatalyseerd door fumarase. Voor een concentratie van 100 mM zijn er veranderingen in temperatuur waargenomen die mogelijk een gevolg zijn van de dehydratie, alhoewel het in strijd is met de definitie van een endotherm proces. Ook is de temperatuursverandering van de oxidatie van 3,3'-diaminobenzidine en L-tyrosine vastgelegd, maar deze lieten geen veranderingen zien die duiden op warmte productie door de oxidatie. De opstelling maakt het mogelijk om spectroscopie uit te voeren tegelijkertijd met thermografie, maar dit is niet getest.

Contents

1	Introduction	1
2	Quantum Cascade Laser	3
2.1	Population inversion in Multiple Quantum Wells	3
2.2	Tuneable external cavity QCL	5
2.3	Setup for spectral acquisition	6
2.3.1	Internal detector	7
2.3.2	Data acquisition	7
2.3.3	External detector	10
3	Specular reflectance spectroscopy	13
3.1	Refraction, Reflection and Reflectance	13
3.2	Infrared absorption	14
3.3	Setup and Beam Displacement	15
3.4	IR spectrum of Ethanol	19
3.5	Setup improvement	19
4	Spectroscopic imaging of enzyme catalyzed reactions	23
4.1	Catalysed reversible dehydration of L-malate	23
4.2	Oxidation of L-tyrosine and DAB	24
4.3	Experimental setup and measurement method	25
4.4	Spectroscopic imaging of the dehydration of L-malate catalysed by fumarate	27
4.5	Thermal imaging of the oxidation of DAB and L-tyrosine	29
5	Conclusion and outlook	31
	Appendices	35
A	Project description	36

CONTENTS

B	Ethanol spectra for different concentrations	38
C	Thermal recordings of enzymatic reactions	39

1. Introduction

Chemical reactions happen all around us. It is the production of oxygen via photosynthesis that allows us to breathe, while also numerous reactions take place that are lethal to humans, yet together keeps the balance we call nature. Scientists continue exploring this delicate balance on an advanced level, sometimes just for understanding, mostly for creating innovative solutions for any challenge science is encountering. Insight into physical processes that can possibly advance our understanding of how the world around us functions is necessary for progress. With this in mind new technologies and methods keep being developed to unravel puzzles and explain phenomena observed in nature.

One method of enhancing knowledge of chemical compounds is spectroscopy. Spectroscopic studies can give qualitative and quantitative information on a compound. Using the right protocol, spectroscopy can provide data on the presence and concentration of chemicals of interest, and therefore it can provide information useful for any kind of purpose, e.g. a diagnosis based on biomarker concentrations indicating diseases such as asthma [1–3]. More specifically, infrared (IR) spectroscopy exploits the interaction between atoms and molecules, and IR electromagnetic waves. Therefore IR spectroscopy can be used to determine the presence and concentration of specific chemicals absorbing, reflecting or scattering electromagnetic radiation in the IR part of the electromagnetic spectrum.

Infrared imaging is typically used for thermal vision, i.e. visualising heat radiation by a certain object. Nowadays it is used for military purposes [4], inspection of thermal insulation [5], etc. At the Delft University of Technology a new master’s project is proposed on monitoring enzymatic reactions using IR imaging and IR specular reflectance spectroscopy simultaneously, since almost no experiments are known that simultaneously measure heat production and concentration of reactants. The combination of specular reflectance spectroscopy and thermal imaging in the wavenumber range of 833 to 1263 cm^{-1} is truly unique in the world of enzyme assays, and might therefore suggest a new method of measuring the performance of enzyme assays. Since reflectance is used instead of transmission, this project may possibly even provide a new way of identifying chemicals on thin films, useful for instance in forensic science.

Enzymes are biological catalysts, molecules that increase the reaction rate of a specific reaction, without being consumed in the reaction themselves. An example of an enzyme is lactase, which stimulates the hydrolysis of lactose into galactose and glucose, and is insufficiently present in lactose-intolerant people [6]. The main goal of the project is to design an IR imaging system to monitor enzymes in action, while simultaneously performing IR spectroscopy. Theoretically such an experiment can monitor the amount of heat produced by a catalysed reaction while at the same time provide information about the concentration of the chemicals playing a role in the reaction. Together this can provide spectroscopic data as well as thermal data by performing only

one experiment.

A good IR source for IR spectroscopy is invaluable. The output spectrum of the IR source plays an important role in the precision of concentration measurements and in the quality of thermal imaging. By those means a *Quantum Cascade Laser* (QCL) will be analysed and discussed. Firstly the physics behind the wide bandwidth of a QCL will be explained. Secondly the design of the QCL used for the experiments will be reviewed. Next the spectrum of the QCL is recorded using the manufacturer's software and a National Instruments digitizer. Lastly the spectrum is recorded using an external detector, and differences between the internal and external spectrum will be discussed.

The third chapter of this thesis will cover the spectroscopic part of this project. Theory on the complex refractive index and its relation to absorbance and reflectance will be discussed. Also IR absorption at atomic and molecular level will be covered. The spectroscopic setup will be explained and its performance will be tested by trying to find the IR spectrum of ethanol. Next enzymes in action will be covered in a new chapter. This chapter will briefly cover enzymatic reactions and reaction rate. The definitive setup will be presented and explained. Results on IR imaging will be presented and the overall performance of the setup will be analysed and discussed.

2. Quantum Cascade Laser

Nowadays a wide variety of lasers are available and are used for many applications ranging from the detection of gravitational waves [7] to clinical breath analysis [8]. Lasers are typically divided by gain medium; one such gain medium, based on materials that can be doped, leads to semiconductor lasers. Semiconductor lasers exploit a semiconductor structure as gain medium and come in various configurations. One of these configurations is the Quantum Cascade Laser (QCL), a semiconductor laser containing several quantum wells in cascade. This chapter will present theoretical information about population inversion in a QCL based on their their configuration, as well as a brief description of the external cavity of the QCL. Furthermore experimental data will be presented regarding the spectrum acquisition. The QCL that is used is a commercial device; the LaserScope by Block Engineering [9], and was previously used at the Optics research group at the Delft University of Technology for breath analysis using infrared spectroscopy [1–3].

2.1 Population inversion in Multiple Quantum Wells

Stimulated emission is a photon amplification process. An incoming photon of energy $h\nu$ stimulates an electron in an energy band E_2 to transit down to the ground state E_1 and emit another photon with energy $h\nu$, hence the name stimulated emission. Fermi-Dirac statistics states that at room temperature the density of electrons in the ground state is much higher than the density of electrons in an excited states [10]. When considering such a two level system it should be taken into account that an incoming photon has an equal probability of exciting an electron from E_1 to E_2 or stimulating photon emission by the transition of an electron from E_2 to E_1 . Therefore photon amplification can only occur if the density of electrons in an excited state is higher than the density of electrons in the ground state [11]. This is called population inversion and for temperatures in the order of room temperature this can only be accomplished by systems with more than two energy levels.

Consider figure 2.1, which shows a thin-layered semiconductor with bandgap energy E_{g2} confined between two oppositely doped semiconductors with bandgap E_{g1} . Note that a quantum well of finite depth is created. The confined layer is only confined in the x -direction. Consequently electrons can be considered free in the yz -plane. When a forward bias is applied, electrons are fed into the n-type semiconductor. Since electrons tend to occupy the lowest available energy state, following Pauli's exclusion principle, the excess electrons in the n-type semiconductor will 'fall' into the well and start occupying the allowed states. Since the electrons are free to move in the yz -plane, electrons are allowed to have energies unequal to those predicted by the one dimensional quantum well model. For this to happen extra energy in the form of kinetic energy E_k in the yz -direction is required. Holes, tending to occupy high energy states, follow a path complementary to that of

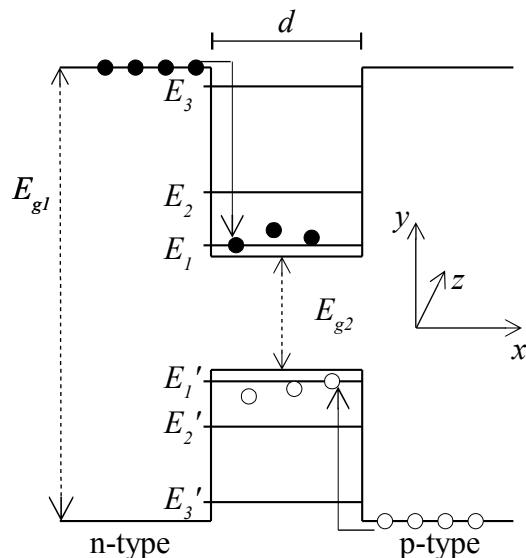


Figure 2.1 – A single quantum well consisting of a small bandgap semiconductor confined between two larger bandgap semiconductors. In cascade these are found in modern laser diodes and LEDs. The solid black dots represent electrons, whereas holes are represented by the white dots. Note that this illustration represents electrons confined in a single direction, thus being free in the perpendicular plane.

electrons, as can be seen in figure 2.1. When electron-hole recombination occurs across E_{g2} , photons are generated with energies $h\nu > E_{g2}$. Such recombinations are called interband transitions. By engineering a structure such that quantum wells are in *cascade*, a multiple quantum well structure is designed. These structures are found in high intensity LEDs and modern laser diodes.

Quantum cascade lasers do not emit radiation produced by interband transitions. The lasing transition in a QCL is the transition between subbands in the quantum well, for instance between E_3 and E_1 in figure 2.1. These transitions are called intersubband transitions. This results in photon energies purely depending on the layer thickness of the quantum well, thus independent of semiconductor material, in contrast to ordinary laser diodes. Consequently lasing action only occurs when a population inversion in the quantum well is created, i.e. more electrons occupy the E_3 state than the E_1 state. In practise this is rather challenging, because excited electronic states inside the quantum well have lifetimes in the order of picoseconds [12, 13].

The working of QCLs will now be further elaborated using figure 2.2, which shows a schematic of one of the first proposed QCLs by Faist et al [14]. The graphs on the subbands represent the probability of the electron as a function of distance: $|\Psi_n(x)|^2$, where Ψ_n corresponds with the wavefunction at subband n . Two specific regions need to be defined: the active region and the digitally graded alloy. The active region are the semiconductor layers where photon emission occurs. The digitally graded alloy regions make sure electrons are injected in the right subband of the active region. The digitally graded alloy regions will be called injector regions.

Following figure 2.2, electrons tunnel extremely fast from the first injector region into the third subband in the active region.^a Electrons live relatively long in this state, in the order of several

^aTunneling is the process of a particle forcing itself through a potential barrier of finite height.

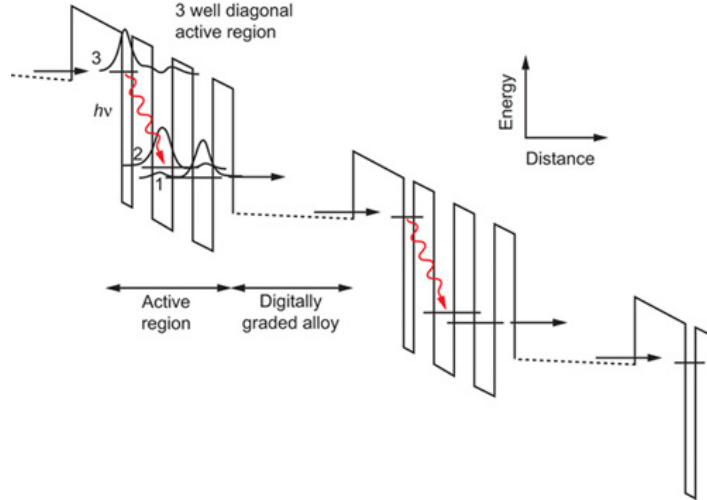


Figure 2.2 – Schematic diagram of one of the first QCLs that was proposed, manufactured and tested by Faist et al [14].

picoseconds. This 'long' lifetime is due to the large transfer of momentum accompanied by a laser transition. Population inversion is created by the significantly shorter lifetime in the second subband in the order of subpicoseconds, due to phonon coupling to the first subband. In addition, the tunneling out of the first subband into the injector region is extremely fast. Electrons in the injector region travel through this region, barely losing energy. Then these electrons can tunnel quickly into the third subband to repeat the described process in the adjacent active region. In conclusion, the whole system can be described as a four level laser system [14].

Modern QCL devices have large bandwidths. Figure 2.2 suggests that the bandwidth increases with the number of subbands in the quantum well. Since modern QCLs can have over ten subbands in their quantum wells, a wide range of wavelengths can be emitted by a QCL [15]. Note that initially electrons will always tunnel from the injector region into the high energy subbands in the first quantum well, allowing many laser transitions to lower subbands. By proper engineering of the semiconductor layers a large bandwidth spectrum can be obtained. Small energy differences between lower subbands can be compensated by confinement in only one direction, thus allowing kinetic energy to overcome the small energy gaps between subbands. Now electrons in the higher subbands can transit to all allowed energies in the energy region of the lower subbands. All these allowed energies together are called an energy band.

2.2 Tuneable external cavity QCL

The QCL that will be used for experiments is the *LaserScope*; an external cavity QCL by *Block Engineering* provided with an internal detector [9] for quick measurements. The external cavity QCL earned its name from the external cavity that allows tuning of output wavelengths. Figure 2.3 shows a typical QCL in an external cavity configuration. As discussed in the previous section, the QCL chip emits electromagnetic energy in pulses and has bandwidth of 430 cm^{-1} , corresponding to a bandwidth of around $4 \mu\text{m}$. A diffraction grating in Littrow configuration is used to tune the laser output.

A blazed grating is in Littrow configuration when radiation of wavelength λ is incident on the

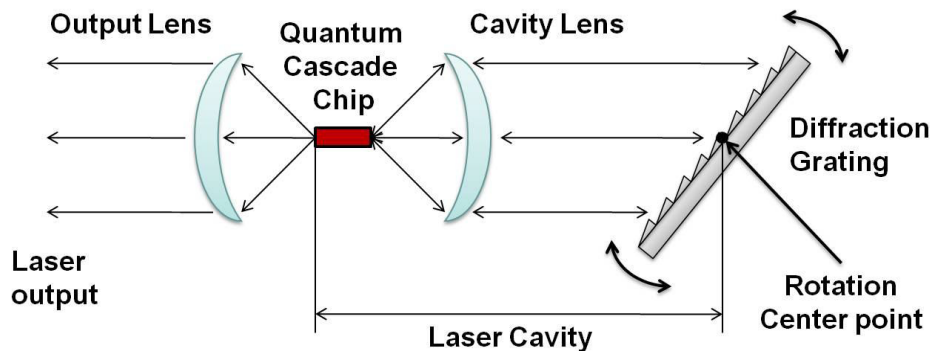


Figure 2.3 – Schematic representation of the QCL used in the experiments [9].

grating at an angle α equal to the angle of diffraction β for order m , see figure 2.4 In this situation $\beta = \theta_B$ is typically called the blaze angle. Let d be the line spacing, such that the blaze angle can be found using

$$\theta_B = \arcsin\left(\frac{m\lambda}{2d}\right) \quad (2.1)$$

which must be equal to the angle of incidence α . When radiation of order zero ($m = 0$) is incident, θ_B should be zero and is therefore independent of wavelength. This means $m = 0$ radiation is reflected by the grating, therefore the grating acts as a mirror along the dashed surface in figure 2.4 for $m = 0$ radiation. For $m = 1$ the blaze angle does depend on λ , hence its use in tuneable lasers like the QCL.

The diffraction grating is typically controlled by a piëzo actuator to control the angle of incidence α . These actuators all have hysteresis, resulting in a voltage range over the actuator where no rotation is performed. In order to improve frequency repeatability this hysteresis needs to be reduced.

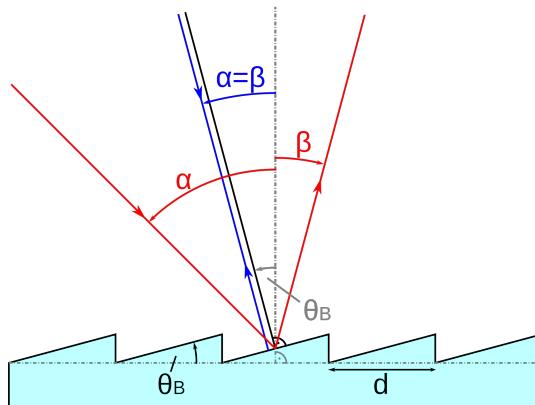


Figure 2.4 – A blazed grating is in Littrow configuration for wavelength λ when $\alpha = \beta = \theta_B$ [16].

2.3 Setup for spectral acquisition

This section will present and discuss results of several experiments with the QCL and the internal and external detector. Firstly the spectrum acquired by the internal detector is presented and discussed. Secondly the spectrum acquired by the external detector is presented and discussed.

Finally explanations are given for differences that were observed between the internal and external detector.

2.3.1 Internal detector

The LaserScope device has an internal Mercury Cadmium Telluride (HgCdTe or MCT) semiconductor detector.^b This detector is coupled to the QCL and therefore can view the intensity as a function of emitted wavelength. The Laserscope software shows the non-calibrated intensity for the whole spectral range of the QCL. From now on this detector will be referred to as the internal detector.

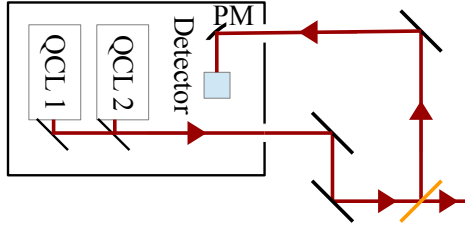


Figure 2.5 – Setup for acquisition of the spectrum using the internal detector. The orange element is a ZnSe beam splitter that reflects five percent of the infrared radiation. A parabolic mirror PM focusses the beam on the detector.

At first the spectrum of the QCL has been acquired using the internal detector. See figure 2.5 for an overview of the setup. The ZnSe beam splitter is used for three reasons. Firstly, the beam splitter allows simultaneous measurements by the internal detector and an external detector. Secondly, the beam splitter allows a visible laser beam to align with the invisible IR beam for guiding purposes. Thirdly, the beam splitter prevents saturation of the internal detector, because it reflects only five percent of its incident IR radiation in the wavelength range of the QCL. The internal detector automatically couples the measured intensity to the corresponding wavenumber $\tilde{\nu}$. Wavenumbers are typically used in IR spectroscopy and are related to the wavelength λ following

$$\tilde{\nu} [\text{cm}^{-1}] = \frac{10^4}{\lambda [\mu\text{m}]} \quad (2.2)$$

The spectrum of the QCL can be found in figure 2.6. A sharp drop is detected around 1010 cm^{-1} . This drop is a result of the device having two separate QCLs, one scanning from approximately 833 cm^{-1} to 1010 cm^{-1} and one scanning from 1010 cm^{-1} to approximately 1263 cm^{-1} . The QCL laser used for the experiments is a pulsed laser. The pulse width was set to 272 ns and the pulse period to 5600 ns. As a result the duty cycle is $\frac{272}{5600} \approx 4.9 \%$.

2.3.2 Data acquisition

Since the LaserScope software provided by Block Engineering limits manipulation of the detection process, individual pulses cannot be displayed by this software. For this an NI PCI-5922 digitizer

^bHg_{1-x}Cd_xTe only becomes a semiconductor for approximately $x \geq 0.2$, where x denotes the fraction of CdTe over the complete HgCdTe material [17].

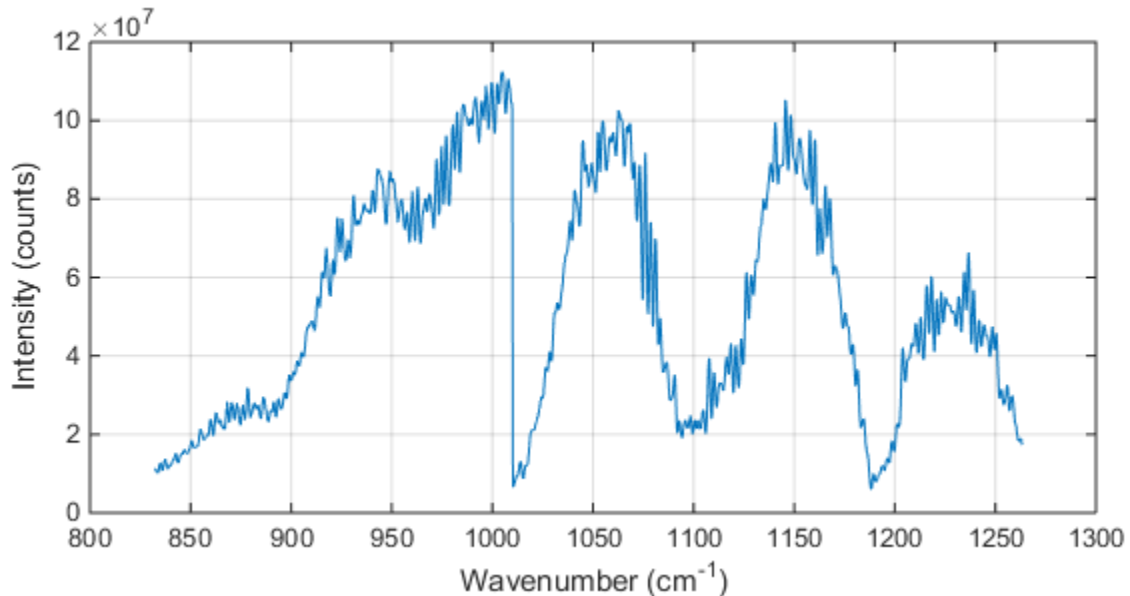


Figure 2.6 – Output spectrum of the QCL acquired by the internal detector, averaged over ten scans. Acquired using the Block Engineering LaserScan software.

is used [18]. The resolution of the digitizer is shown in table 2.1. In order to resolve pulses with a width of 272 ns the temporal resolution of the digitizer should be at least equal to the pulse width, corresponding to a sampling rate of

$$\frac{1}{272} \cdot 10^9 = 3.68 \text{ MS/s}$$

At this sampling rate the resolution is 20 bits, meaning data is being written in the internal buffer at around 9.2 MB/s. Obviously, for higher sampling rates data is written at an even faster rate. The internal buffer is limited in storage size, so for data not to be overwritten the data needs to be transferred from the acquisition card to a data storage device, in this case an SSD. Individual pulses have been detected, as presented in figure 2.7, at a sampling rate of 15 MS/s. However, the data transfer proved to be a bottleneck for acquiring the complete spectrum. The data points were acquired a lot faster than data could be transferred to the SSD, so a queue of data points was formed in the buffer. Since the buffer is limited in storage size, data was overwritten within a second from starting the scan. Because a scan typically takes 6.5 seconds to complete, a workaround was necessary.

Table 2.1 – The resolution of the NI PCI-5922 for different sampling rates [18].

Sampling rate (MS/s)	Resolution (bits)
0.500	24
1	22
5	20
10	18
15	16

A LabVIEW Virtual Instrument (VI) was created by MSc Zhe Hou to only detect peaks above a user-specified voltage threshold [2]. A drawback of this VI is its scanning method; in the software

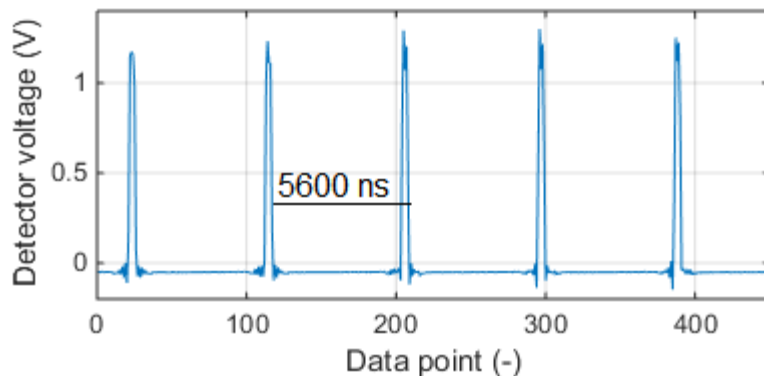


Figure 2.7 – A number of pulses detected by the internal detector at a sampling rate of 15 MS/s. The laser was set to a wavenumber of 1000 cm^{-1} ($\lambda = 10\text{ }\mu\text{m}$).

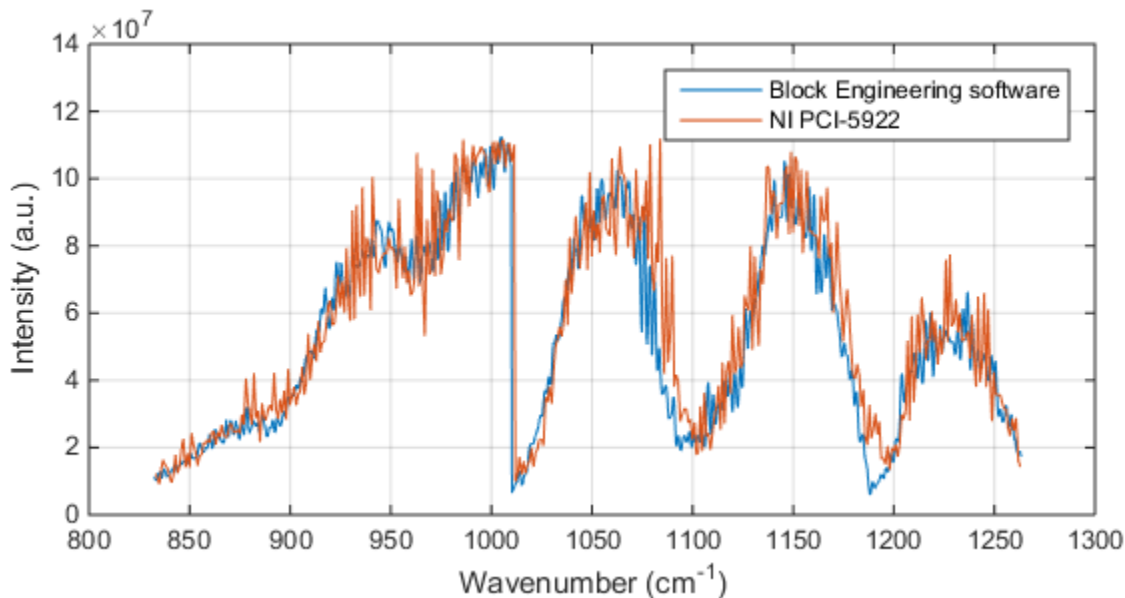


Figure 2.8 – The QCL spectrum acquired by the internal detector for the Block Engineering software and the NI PCI-5922 digitizer.

the wavenumbers are set manually, thus increasing the scan time. However, the VI also gives an extra degree of freedom, namely the scanning range. Users can set the wavenumber range of the scan themselves. All in all this VI slows down the scanning process from around 6.5 seconds to 350 seconds, but solves the acquisition problem and also gives more freedom over the scanning range. In figure 2.8 a comparison is visible between the Block Engineering software scan that took 6.5 seconds, similar to the one in figure 2.6, and the spectrum acquired by the NI PCI-5922 digitizer that took 350 seconds.

The output of the NI PCI-5922 is a voltage, as is shown in figure 2.7. After analysing the shape of the detector voltage vs. wavenumber plot (not presented here) it became clearly visible that the detector voltage is directly proportional to the intensity. The proportionality constant proved to be $8.5 \cdot 10^7\text{ V}^{-1}$. This proportionality constant was used for the comparison in figure 2.8.

2.3.3 External detector

The QCL spectrum has also been acquired by a different HgCdTe detector. This detector, the photovoltaic *PCI-4TE-10.6* detector by *VIGO System S.A.*, is also used to monitor pulses and find the QCL spectrum. Peak performance for the *PCI-4TE-10.6* occurs at $10.6 \mu\text{m}$, and detectivity is considered constant for 8 to $10.6 \mu\text{m}$ ($1250 - 943 \text{ cm}^{-1}$), but decreases exponentially for 10.6 to $12 \mu\text{m}$ ($943 - 833 \text{ cm}^{-1}$) [19], suggesting more noise for these wavenumbers.

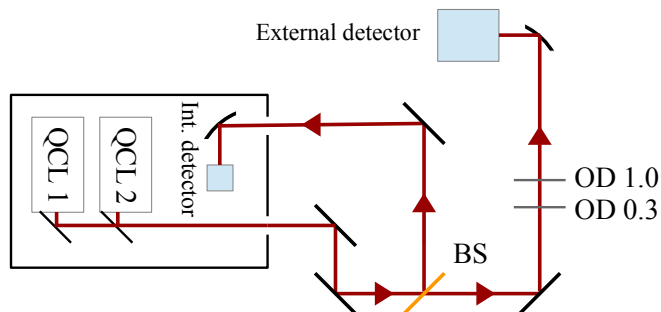


Figure 2.9 – Setup for spectrum acquisition by the external detector.

The setup for acquiring the QCL spectrum using the internal and external detectors simultaneously can be found in figure 2.9. The beam passes through two neutral-density (ND) filters, one with an optical density (OD) of 0.3 and one with an OD of 1.0. The OD is related to the fraction of intensity of the beam that is transmitted I over the incident intensity I_0 following

$$\frac{I}{I_0} = 10^{-\text{OD}} \quad (2.3)$$

hence the total attenuation of the filters together is $\frac{I}{I_0} = 10^{-1.3} \approx 5 \%$. Since only 95 % of the

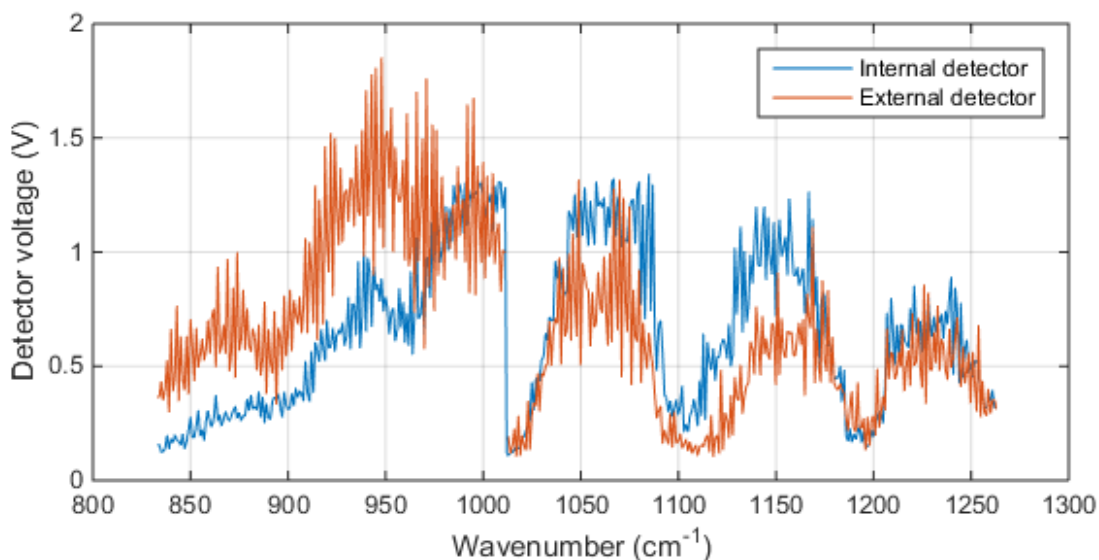


Figure 2.10 – Simultaneous measurement of the spectrum using both detectors.

energy incident on the beam splitter is transmitted, a total of $\approx 4.8\%$ reaches the parabolic mirror in front of the external detector. The parabolic mirror focusses the beam on the detector, similar to the parabolic mirror in front of the internal detector. This setup proved to be the most convenient and reliable way of comparing the output of the internal and external detector simultaneously.

Figure 2.10 shows that the internal and external detector record roughly the same shape. However, some differences are observed. The signal-to-noise ratio (SNR) of the spectrum detected by the external detector is significantly lower than that of the internal detector, most likely due to the presence of the extra ND-filters. Also a Fabry-Pérot effect occurs in between the two filters, possibly causing extra noise. Slightly rotating a filter resulted in major differences in output voltage, but it should decrease the Fabry-Pérot effects. Using the LaserScope's internal software it was verified that the attenuation of the ND-filters is constant for the spectral range of the QCL.

Although the shape recorded by the internal and external detector are roughly the same apart from the noise, other differences are observed. The external detector voltage for $833 - 1010\text{ cm}^{-1}$ is higher than the internal detector voltage, but for $1011 - 1263\text{ cm}^{-1}$ it is slightly less. This could be explained by differences in spectral responsivity. This data is not available for both detectors. In practice it was noticed that the detectors have different saturation levels, making it more likely there are differences in spectral responsivity. Later experiments suggested that the differences could also possibly be caused by beam displacement, i.e. the beam spot position on the external detector varies with the wavenumber. This issue of displacement will be discussed in more detail in section 3.3.

3. Specular reflectance spectroscopy

Specular reflectance spectroscopy uses the spectrum of the specular reflected radiation from a sample surface to identify the sample. A major advantage of reflectance spectroscopy is its short path-length in the sample, allowing better spectroscopic results for heavily absorbing samples. Nowadays reflectance spectroscopy is used in chemical physics and biophysics, and is commonly applied in forensic science [20] and used for spectroscopy on thin films [21]. This chapter will cover theory on why IR radiation can be absorbed and what the consequence is for the spectrum. Next the setup will be presented, and the spectrum of ethanol will be measured for testing the setup. Then an improved setup will be presented. Last an alternative way of calculating the spectrum of ethanol is presented alongside a measurement using this new calculation method.

3.1 Refraction, Reflection and Reflectance

Electromagnetic (EM) waves propagating in the z -direction have an electric field oscillating in the x - or y -plane. Molecules of a dielectric medium polarize due to these oscillations. This polarization effect is not lossless and is described in terms of a complex relative permittivity

$$\varepsilon_r(\tilde{\nu}) = \varepsilon_r'(\tilde{\nu}) - j\varepsilon_r''(\tilde{\nu}) \quad (3.1)$$

where ε_r' and ε_r'' denote respectively the real and imaginary part of the relative permittivity [11]. The real part, ε_r' , provides information on the polarization without considering losses, whereas the imaginary part, ε_r'' , only considers losses. Both the real and imaginary part of the relative permittivity are wavenumber dependent.

A result of Maxwell's EM wave equations is that for non-magnetic media the refractive index n can be written as

$$n(\tilde{\nu}) = \sqrt{\varepsilon_r(\tilde{\nu})} \quad (3.2)$$

where we take in account the wavenumber dependency of the complex relative permittivity ε_r . Due to the complex notation of ε_r , the refractive index is described in complex terms as well. Therefore the complex refractive index n can be written as

$$n(\tilde{\nu}) = n'(\tilde{\nu}) - jn''(\tilde{\nu}) \quad (3.3)$$

By using this equation and substituting equation (3.1) in equation (3.2)

$$n(\tilde{\nu}) = n'(\tilde{\nu}) - jn''(\tilde{\nu}) = \sqrt{\varepsilon_r'(\tilde{\nu}) - j\varepsilon_r''(\tilde{\nu})} \quad (3.4)$$

is obtained. n' is called the refractive index and n'' is typically referred to as the extinction coefficient. Now ε_r' and ε_r'' can be written in terms of refractive index n' and extinction coefficient

n'' , and vice versa. Note that ε_r' and ε_r'' are wavenumber dependent, so n' and n'' are wavenumber dependent as well. Although it seems obvious, the wavenumber dependence is actually of vital importance, since that is what makes the spectroscopic fingerprints of compounds unique.

Fresnel's equations describe the reflection and transmission of the electric field at a boundary of two media [11]. Consider two types of polarized electromagnetic waves: transverse electric (TE) and transverse magnetic (TM) polarized waves, E_{\perp} and E_{\parallel} respectively. The reflection coefficients r_{\perp} and r_{\parallel} for these polarizations are defined as

$$r_{\perp}(\tilde{\nu}) = \frac{E_{r0\perp}(\tilde{\nu})}{E_{i0\perp}(\tilde{\nu})} = \frac{\cos \theta_i - \sqrt{n^2(\tilde{\nu}) - \sin^2 \theta_i}}{\cos \theta_i + \sqrt{n^2(\tilde{\nu}) - \sin^2 \theta_i}} \quad (3.5)$$

$$r_{\parallel}(\tilde{\nu}) = \frac{E_{r0\parallel}(\tilde{\nu})}{E_{i0\parallel}(\tilde{\nu})} = \frac{\sqrt{n^2(\tilde{\nu}) - \sin^2 \theta_i} - n^2(\tilde{\nu}) \cos^2 \theta_i}{\sqrt{n^2(\tilde{\nu}) - \sin^2 \theta_i} + n^2(\tilde{\nu}) \cos^2 \theta_i} \quad (3.6)$$

for angle of incidence θ_i . Note that n in (3.5) and (3.6) is the ratio of the refractive index of the initial (n_1) and second medium (n_2), so $n = \frac{n_2}{n_1}$ and is wavenumber dependent.

Reflectance R is defined as

$$R(\tilde{\nu}) = |r(\tilde{\nu})|^2 = \left| \frac{E_{r0}(\tilde{\nu})}{E_{i0}(\tilde{\nu})} \right|^2 = \frac{I_{r0}(\tilde{\nu})}{I_{i0}(\tilde{\nu})} \quad (3.7)$$

If the initial medium is air, n_1 can be considered unity, so $n = n_2$ is the refractive index of the reflecting medium. The reflectance for both TE and TM polarization are simply found by squaring equations (3.5) and (3.6). This shows that the intensity of the reflected beam depends on the polarization of the incident beam, the complex refractive index of the reflecting medium, and the angle of incidence. As a conclusion, the reflectance responds to changes in refractive index caused by absorption.

Specular reflectance spectroscopy differs from the more ordinary absorption spectroscopy in some important ways. In absorption spectroscopy the absorbance \mathcal{A} depends on extinction coefficient ϵ , concentration c and path length l following the Beer-Lambert law

$$\mathcal{A}(\tilde{\nu}) = -\log \left(\frac{I(\tilde{\nu})}{I_0(\tilde{\nu})} \right) = \epsilon cl \quad (3.8)$$

However, in specular reflectance spectroscopy the ratio $\frac{I}{I_0}$ is not proportional to concentration in this sense. A valid way of extracting the concentration in specular reflectance spectroscopy can be done using the Kramers-Kronig method [22]. For the sake of simplicity this method will not be presented and used in this thesis. Rather, a new quantity is introduced: \mathcal{R} . It is defined as

$$\mathcal{R}(\tilde{\nu}) = -\log(R) = -\log \left(\frac{I_R(\tilde{\nu})}{I_0(\tilde{\nu})} \right) \quad (3.9)$$

where I_R is the reflected intensity from the sample. \mathcal{R} will be referred to as the logarithmic reflectance. As a result of this alternative way of defining the absorbance only qualitative conclusions can be drawn from spectroscopic data that is to be presented, but it also gives rise to the opportunity of comparing measurements with spectra found by absorption spectroscopy.

3.2 Infrared absorption

Infrared radiation is all electromagnetic radiation having a wavelength between 700 nm and 1 mm, corresponding with wavenumbers between 14286 cm^{-1} and 10 cm^{-1} . All objects having a

temperature higher than zero Kelvin emit infrared radiation, obeying Planck's law. This makes infrared detectors in general more susceptible to background radiation than visible light detectors.

As explained in the previous section, the complex refractive index changes for absorption peaks. All EM radiation may be absorbed by matter, yet the cause of absorption is not the same for every case. UV and visible radiation is absorbed by an atom or molecule when an electron transits from a state with principal quantum number $n = i$ to a state $n = i + j$ where $j \in \mathbb{N}$ and $j \neq 0$. IR radiation does not have enough energy to cause such transitions.^a Rather, absorption of infrared radiation causes the vibrational and rotational degrees of freedom of the molecule to be excited.

Atoms in molecules can be subject to different vibrational motions. The six different motions are called vibrational modes and are presented in figure 3.1. Common molecules used for visualising these vibrations are CO_2 and H_2O , but many more molecules can vibrate in those modes. As stated before, every molecule has its own unique spectroscopic fingerprint. What makes the vibrational modes unique is the wavenumber they occur at. As an example, the symmetrical stretch vibrations for CO_2 and H_2O occur at different wavenumbers, hence a different spectrum is observed. In terms of complex refractive index one could state that the complex refractive index changes as a result the absorption of radiation. This change leads to a difference in reflection, as can be seen in equations (3.5), (3.6) and (3.7).

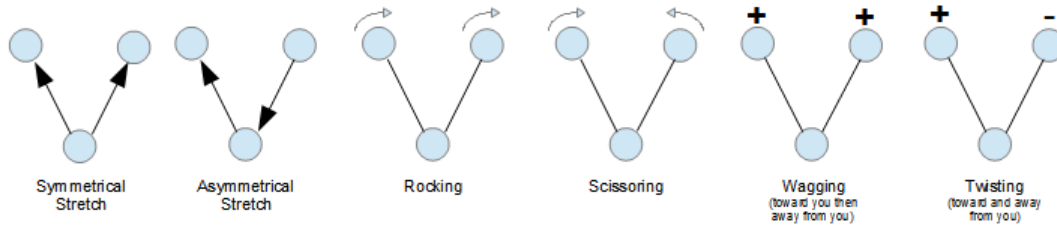


Figure 3.1 – The vibrational modes that occur when IR radiation is absorbed [23].

3.3 Setup and Beam Displacement

Figure 3.2 shows the spectroscopic setup. As discussed in section 2.3.1, the beam splitter reflects five percent of its incident radiation, and therefore prevents saturation of the internal detector. The beam splitter also acts as a window for the HeNe guiding laser beam. Using two pinholes the IR beam and the guiding beam are positioned so that they overlap. Next the beam is elevated using the periscope. A parabolic mirror with a focal length of 152.4 mm focusses the beam on the next mirror, after which it starts diverging, creating a larger spot size on the sample. The IR beam is incident on the sample at an angle of $\theta_i \approx 45^\circ$ with respect to normal. Then the beam is focussed on the detector by a +150 mm lens.

For the sake of testing the beam alignment the spectrum of the QCL was recorded using a silver mirror as sample in figure 3.2, so theoretically the internal and external detector should have negligible differences when the mirrors are considered to have nearly 100 % reflectance and two ND filters, having an OD of 1.3 together, are placed in front of the detector. In practice however,

^aThe energy threshold at which such transitions occur are different for every atom and molecule, so it is not impossible that those transitions happen for IR radiation.

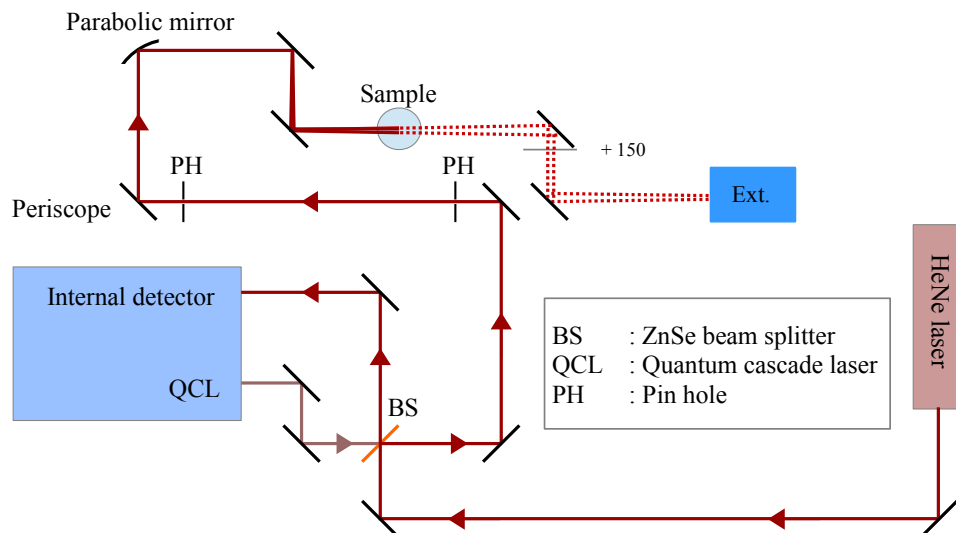


Figure 3.2 – Setup for imaging heat radiation. The guiding beam is shown in red. Note that the illustration is not to scale.

this not the case, as figure 3.3 suggests. The ND filter with an OD of 0.3 was removed for this measurement as to increase the detector voltage. Nevertheless, for wavenumbers between 900 cm^{-1} and 970 cm^{-1} , and between 1100 cm^{-1} and 1200 cm^{-1} , dramatic differences are observed. For the latter region, no peaks were detected at all. Observation of the beam for those wavenumbers proved that beam displacement was responsible for those differences. MSc Vincent Docter found similar displacement in a different setup using the same QCL device and described it in his Master thesis [24].

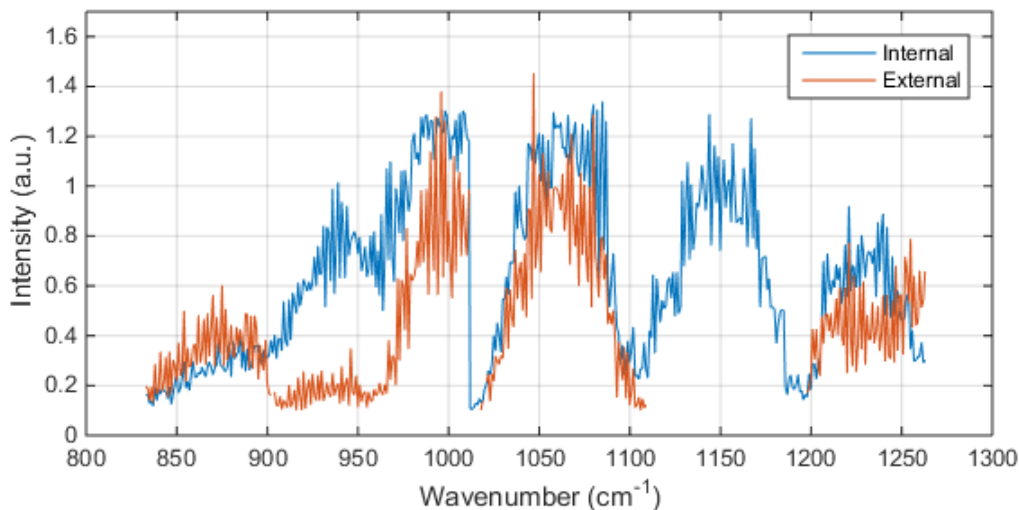


Figure 3.3 – Spectrum recorded by internal and external detector, using the setup presented in figure 3.2. For finding the reference spectrum, a mirror was used as sample and an OD 1.0 filter was placed in front of the external detector to prevent saturation.

Table 3.1 – The six spectral regions of the QCL that required alignment at different wavelengths.

Region number	Spectral region (cm^{-1})	Alligned for wavenumber (cm^{-1})
1	833 - 893	870
2	894 - 967	932
3	968 - 1009	1000
4	1011 - 1108	1060
5	1109 - 1198	1150
6	1199 - 1250	1225

In order to work around the beam displacement the external detector was mounted on a 3D translational stage so its position could be adjusted manually. This meant the position of the external detector needed to be changed for the previously described wavenumber intervals. Analysing figure 3.3 resulted in the conclusion that the spectrum needed to be divided in six spectral regions, each requiring a different alignment, see table 3.1. In practice it was noticed that the first and third spectral region require a similar alignment, which agrees with Vincent Docter’s results. For completing a scan by manually adjusting the external detector’s position, first the detector is aligned for 1000 cm^{-1} . Next the detector voltage, which is directly proportional to the intensity, is acquired as presented in section 2.3.2 for the first and third spectral region. Next the detector is aligned for 932 cm^{-1} and a scan over the corresponding wavenumber interval is performed. After that the same was done for the fourth, fifth and last region. Afterwards the six separate data files that are recorded are bundled to create one file containing the whole QCL spectrum. A complete scan took approximately 15 minutes. Ten of those complete scans were performed, and the result is presented in figure 3.4. In figure 3.4 the darker blue line is the spectrum averaged over ten scans, whereas the shaded blue peaks indicate the standard deviation. In conclusion, this method results

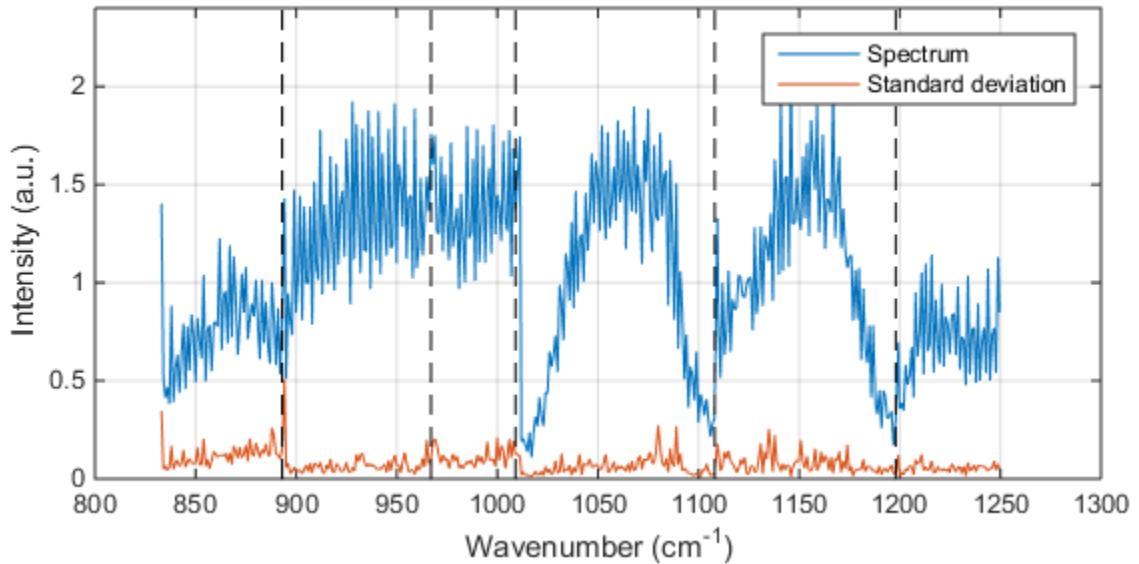


Figure 3.4 – Spectrum of the QCL by manually adjusting the position of the external detector. The spectrum averaged over ten scans is shown in blue, and the standard deviation is shown in orange. The dashed vertical lines divide the spectral regions.

in similar spectra for the internal and external detector, but the manual adjustments counteract repeatability.

The time it takes for a scan to complete increased drastically and repeatability decreased as well, but many similarities with the internal spectrum were observed, as can be seen by analysing figures 3.3 and 3.4. This gave rise to the idea that piezoelectric actuators could improve repeatability by adjusting the angle of the mirrors. Consequently piezoelectric actuators were implemented in the mirrors directly before and after the beam splitter, i.e. the second and third mirror seen from the laser exit port for the beam that is transmitted by the beam splitter. Immediately it was noticed that the external detector saturated due to the more refined alignment. For this reason the OD 0.3 filter was placed in front of the detector once again, together with the OD 1.0 filter that was already there for acquiring the data in figures 3.3 and 3.4. Considering the losses from all the mirrors, including the mirror simulating a sample, the intensity incident on the external detector should be significantly less than the intensity at the internal detector. The total loss of light γ depends on the number of mirrors N the beam reflects on, the factor of light loss κ at the beam splitter and the loss by ND filters following equation (2.3), following

$$\gamma = \kappa \cdot (0.97)^N \cdot 10^{-OD} \quad (3.10)$$

where 0.97 is the reflectance of the silver and gold-plated parabolic mirrors [25]. The total loss for the beams incident on the internal and external detector, γ_{int} and γ_{ext} respectively, are 4.4 % and 3.4 %. In contrast to what these attenuations suggest, the external detector showed a higher output voltage than the internal detector, as presented in figure 3.5. This could be due to differences in spectral response, more efficient focussing of the beam onto the detector and inaccuracy in the reflectance of the mirrors. Additionally the two ND filters cause an increase in noise and can also give rise to a Fabry-Pérot effect.

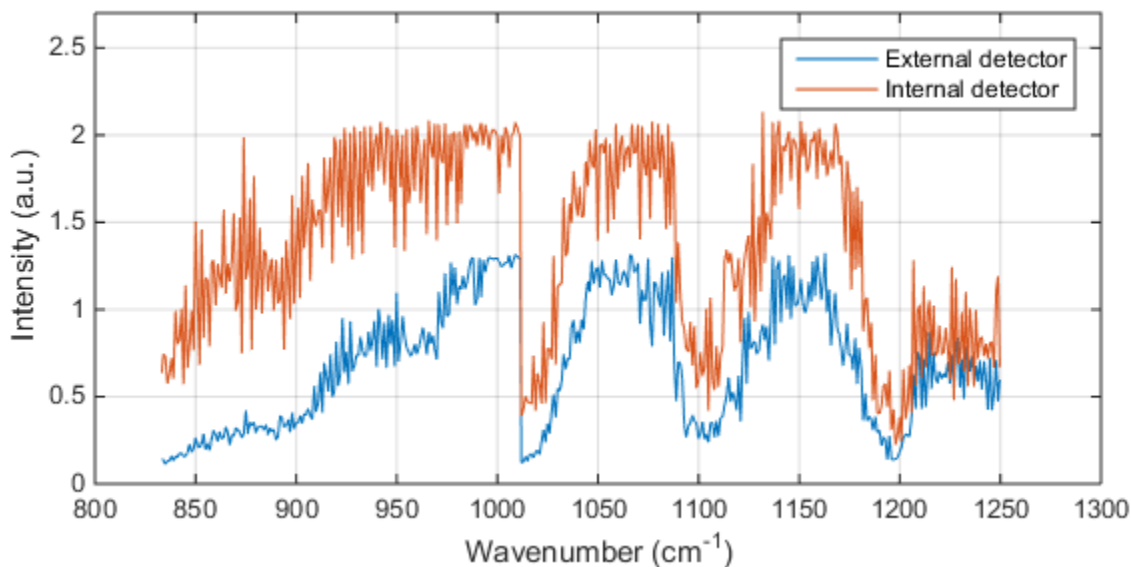


Figure 3.5 – QCL spectrum with piezo compensation. The external detector is slightly saturated for $920 - 1010 \text{ cm}^{-1}$ and for the peaks around 1060 and 1150 cm^{-1} .

3.4 IR spectrum of Ethanol

Ethanol has three major absorption peaks in the wavenumber range of the QCL, therefore ethanol is used to test the performance of the setup. The spectrum of ethanol in figure 3.6 was recorded following the procedure explained in the previous section. The logarithmic reflectance \mathcal{R} is calculated by taking the 10-based logarithm of the ratio of external and internal detector voltage U , so

$$\mathcal{R}(\tilde{\nu}) = -\log\left(\frac{U_{ext}(\tilde{\nu})}{U_{int}(\tilde{\nu})}\right) \quad (3.11)$$

In figure 3.6 the orange line is the spectrum according to the PNNL database and is optimised for absorption spectroscopy, so only a qualitative comparison can be made. The peak ranging from 1000 cm^{-1} to 1130 cm^{-1} is clearly visible and is due to C-O stretching vibrations. The drop at around 1011 cm^{-1} is due to the QCL device switching from the first to the second laser. Around 890 cm^{-1} a peak is detected as well. Although this peak overlaps with a peak from the PNNL database, it might be possible that it is an artefact, because it could correspond to the dip that is visible at the same wavenumber for the external detector in figure 3.5. No voltages were recorded for $\tilde{\nu} > 1200\text{ cm}^{-1}$, which can also be explained by referring back to figure 3.5, because for $\tilde{\nu} > 1200\text{ cm}^{-1}$ the intensity is approximately the same for both detectors, yet for the other wavenumbers the intensity at the external detector is approximately twice that at the internal detector.

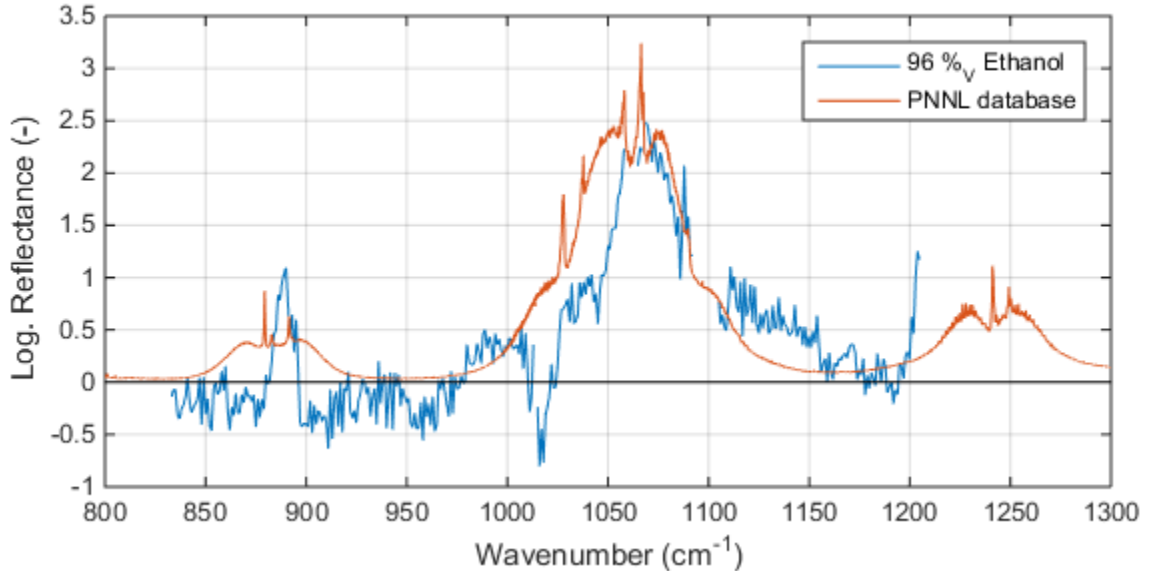


Figure 3.6 – The spectrum of ethanol, acquired following the procedure presented in section 3.3. The orange line shows the data according to the PNNL database and is only shown for a qualitative comparison. It can be observed that the wavenumber axis is not calibrated.

3.5 Setup improvement

Since the aim of the project is to perform spectroscopy and thermography of an enzymatic reaction simultaneously, it is important that performing a scan has a high repeatability and can be done

quickly. Although the results in figure 3.6 are fairly promising, the time it takes for such a scan to complete (± 20 minutes) is simply too much, as the reactions of interest finish in a couple of minutes. Also, because manual adjustments are made in between the measurements, the repeatability is low. In the improved setup the repeatability is improved by more efficient focussing of the beam onto the external detector. This was done by placing a parabolic mirror with $\text{rfl} \approx 60$ mm in front of the external detector, so the beam waist in the focal plane is decreased. A comparison between the old and improved setup can be found in figure 3.7.

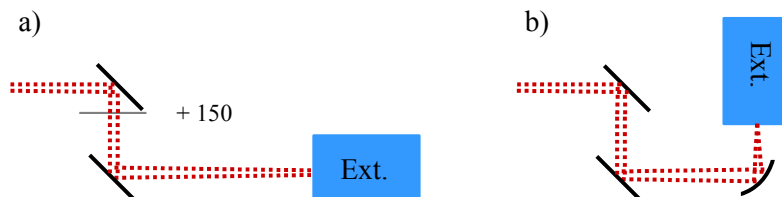


Figure 3.7 – Comparison between the **a)** old and **b)** improved setup.

In addition to using the parabolic mirror, a new method of measuring is introduced. First water is used as a reference sample, since it shows no major absorption compared to ethanol. The external detector is realigned for maximum output voltage of the external detector at 932 cm^{-1} . When the right alignment is set, it is vitally important that the alignment does not change. Now a scan can be performed. Next the compound of interest can be used as a sample. As mentioned before, the alignment should not be changed. Therefore data is collected correctly only if the surface level for water and sample is equal.

Let α and β be the ratio of the external and internal detector voltage for water and the sample respectively:

$$\alpha(\tilde{\nu}) = \frac{U_{\text{water}}(\tilde{\nu})}{U'_{\text{int}}(\tilde{\nu})} \quad (3.12)$$

$$\beta(\tilde{\nu}) = \frac{U_{\text{sample}}(\tilde{\nu})}{U''_{\text{int}}(\tilde{\nu})} \quad (3.13)$$

Although the internal voltage will be similar for all measurements, it will not be exactly the same, hence U'_{int} and U''_{int} . Taking this into account the logarithmic reflectance becomes

$$\mathcal{R}(\tilde{\nu}) = -\log\left(\frac{\beta(\tilde{\nu})}{\alpha(\tilde{\nu})}\right) \quad (3.14)$$

An important advantage of this definition is that the logarithmic reflectance is less susceptible to noise.

A solution of 19.2 % ethanol in water is used to test the improvements, see figure 3.8. An offset is clearly visible and is most likely due to the fact that water reflects less than ethanol. The peak around 880 cm^{-1} is again visible in the improved method, making it less likely to be an artefact. Similar to the results in figure 3.6 a relatively huge reflectance is measured for $1200 - 1263 \text{ cm}^{-1}$, and although a peak should be detected in this region, it is out of proportion when compared with the peaks around 880 and 1050 cm^{-1} . In appendix B ethanol spectra are presented for different concentrations. A conclusion that can be drawn from those spectra is that the concentration seems

to have no clear relation with the peaks in reflectance, as the radiation does not penetrate the liquid. In these cases other techniques should be used to determine concentration if needed.

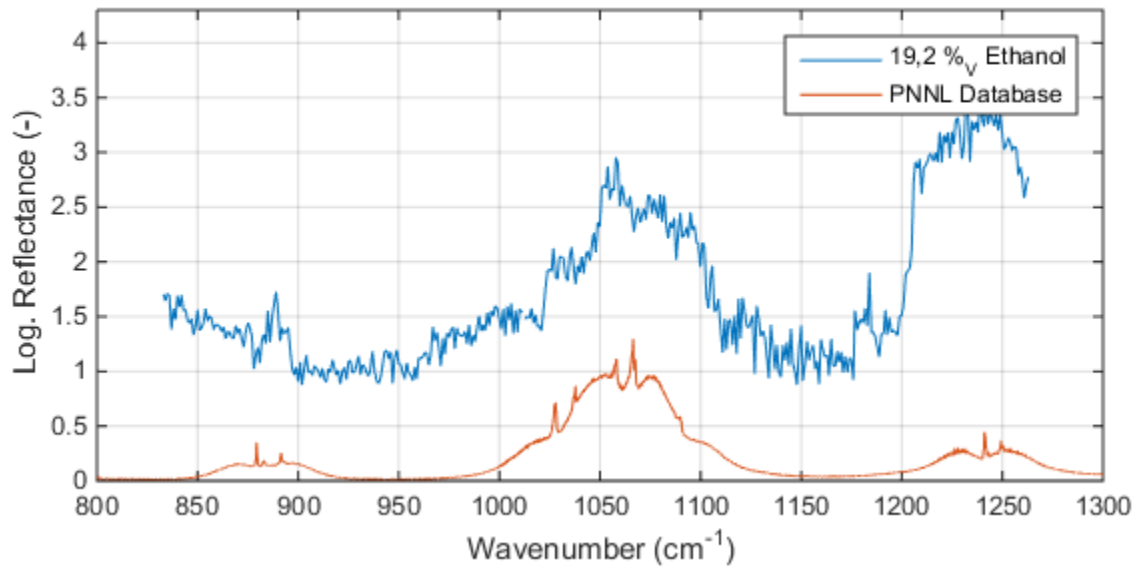


Figure 3.8 – Ethanol spectrum using the improved setup.

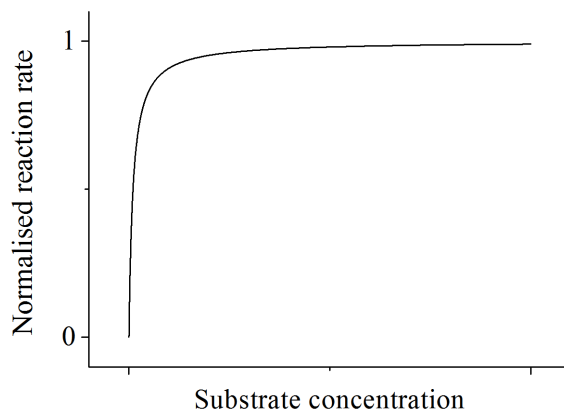


Figure 4.2 – A plot of the Michaelis-Menten equation. Note that the y -axis is normalised.

the involved molecules. The square brackets indicate concentrations. Note that equation (4.1) is obtained by subtracting 'blank rates', i.e. product formation without help of the enzyme is subtracted. The reaction rate $\left(\frac{[P]}{\Delta t}\right)$ as a function of substrate concentration ($[S]$) is plotted in figure 4.2 and gives an idea of the shape of such plots. Taking the limit of equation (4.1) for $[S]$ going to infinity and applying l'Hôpital's rule yields that the maximum reaction rate is indeed v_{max} . Thus, if the y -axis in figure 4.2 would not have been normalised, the curve would have a horizontal asymptote at $\left(\frac{[P]}{\Delta t}\right) = v_{max}$. In contrast to the relation between substrate concentration and reaction rate the reaction rate is directly proportional to the enzyme concentration, i.e. doubling the enzyme concentration doubles the reaction rate.

4.2 Oxidation of L-tyrosine and DAB

L-tyrosine (Tyr, $C_9H_{11}NO_3$) is an amino acid that often occurs in proteins responsible for signal transduction in the human nervous system. It is found in high-protein foods like dairy products, nuts and seeds. The oxidation (fig. 4.3) produces a transparent solution, so the reaction is not visible for the human eye. L-tyrosine and its oxidation is used for testing whether enzyme catalyzed reactions are detectable by thermal cameras.

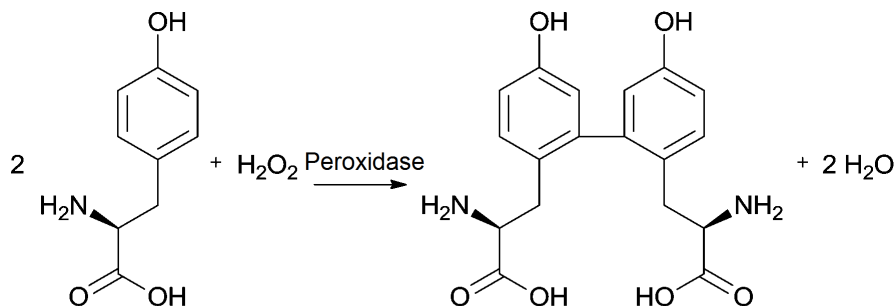


Figure 4.3 – Oxidation of tyrosine catalysed by peroxidase.

3,3'-diaminobenzidine (DAB, $C_{12}H_{14}N_4$) is a chemical compound often used in immunocytochemistry and is oxidized by hydrogen peroxide (H_2O_2), producing a dark-brown reaction product. The reaction can be catalysed by enzyme peroxidase. Since a dark-brown product is formed, it can be easily confirmed whether the reaction is taking place. From a spectroscopy perspective the oxidation can be monitored by UV-VIS spectroscopy as a result of the color change. Applications in practice vary from the detection of fingerprints in blood [29] and for modelling Alzheimer's disease by monitoring plaques [30]. In this project the oxidation of DAB and L-tyrosine is solely used because these are known as exothermic reactions, whereas the dehydration of L-malate is endothermic.

4.3 Experimental setup and measurement method

Since the dehydration of L-malate is an endothermic reaction, energy in the form of heat is consumed. An IR camera can be used to observe the temperature course of the reaction. The definitive setup of the project is presented in figure 4.4. An IR camera is used to image a microtiter plate from the top. In this experiment two cameras were used; the FLIR A655sc and A6753sc [31, 32]. A number of wells are filled with substrate (L-malate). In some of these wells enzymes are added as well, in the remaining wells with substrate a buffer is added. In this case the buffer is 50 mM Tris in water at pH 8, and does not influence the reaction rate. Meanwhile the FLIR camera, in combination with FLIR's ResearchIR software, records the reaction at a user-specified frame rate. The FLIR ResearchIR software allows direct measurement of the temperature, so no calibration is needed.

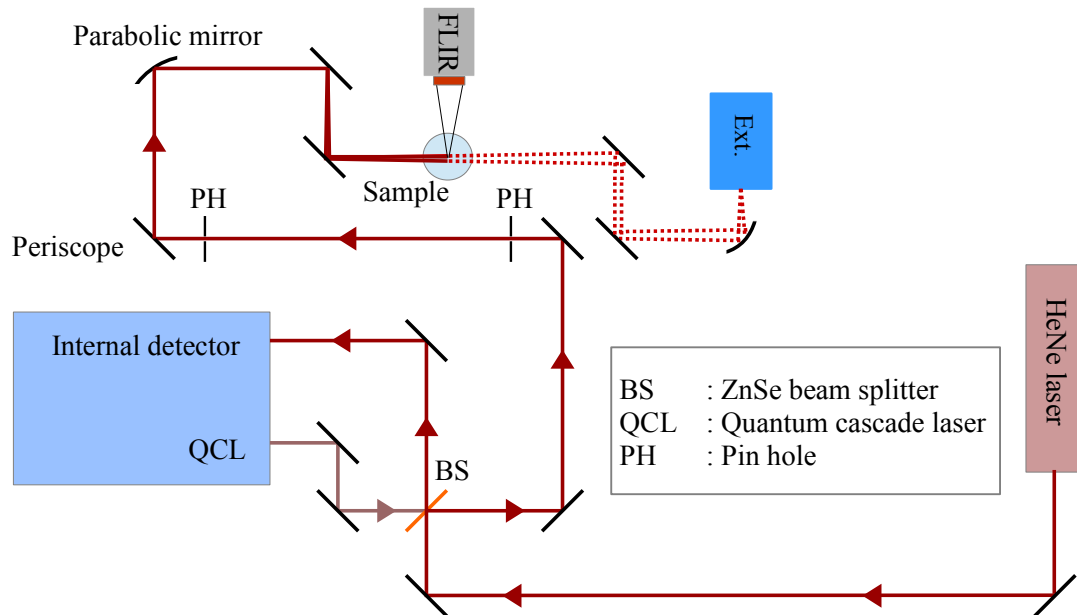


Figure 4.4 – Definitive setup. A FLIR A655 IR camera is used to observe the sample from the top.

A screenshot of a recording can be seen in figure 4.5. In this example four wells are filled with 300 μ L 100 mM L-malate in buffer (50 mM Tris in water at pH 8), and have been resting for around fifteen minutes to reach a stable temperature. Next a small volume of buffer at ambient temperature

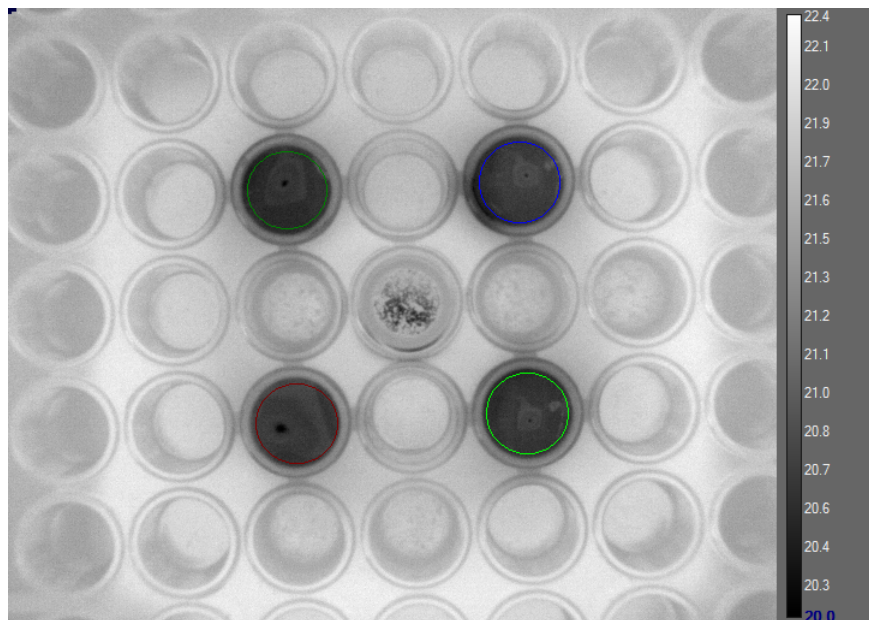


Figure 4.5 – Camera view on the microtiter plate. Note the coloured ROIs that contain the pixels over which averaging has been performed.

is added. After doing so, the recording is started, meaning the average temperature value of all pixels in individual ROIs (regions of interest) is calculated for every frame in the recording. After several tens of seconds enzyme is added to two wells containing buffer and substrate. The recording is manually stopped when a stable temperature is reached again. In conclusion the temperature difference ΔT is calculated by subtracting the average temperature of a reference, non-enzyme containing well \bar{T}_{Ref} by an enzyme containing well \bar{T}_E , so

$$\Delta T = \bar{T}_E - \bar{T}_{Ref} \quad (4.2)$$

In the middle well in figure 4.5 major reflection of the camera itself is visible, hence it's not used as a measurement well. The four measurement wells were chosen following their lack of shadow effects and reduced camera reflection, although the reflection is still clearly visible on the fluid surfaces. All measurement wells are separated by at least one empty well, reducing mutual heat transfer

Figure 4.4 shows that specular reflectance spectroscopy and thermal imaging can be performed simultaneously. However, performing spectroscopy over a user-specified wavenumber range takes time. Every wavenumber that has to be scanned adds a little less than a second to the scanning time. In order to monitor the concentrations of the compounds of interest with increased temporal resolution the scanning time needs to decrease. MSc. Adonis Reyes-Reyes has created a VI-MATLAB code combination that is capable of scanning the complete QCL range in 8 seconds [33], thus can potentially increase the temporal resolution from around 350^{-1} s^{-1} to 8^{-1} s^{-1} . This method has not been used for the experiments, but allows for faster scanning in future experiments and therefore higher temporal resolution. Alternatively the scanning range can be changed to record only for wavenumbers that should show a peak for the product or substrate. However, for this more research needs to be carried out as to where those peaks should be in the $833 - 1263 \text{ cm}^{-1}$ range.

4.4 Spectroscopic imaging of the dehydration of L-malate catalysed by fumarate

Specular reflectance spectroscopy has been performed on 5 mL 100 mM L-malate in buffer, resulting in the spectrum in figure 4.6. Since information on the reflectance/absorbance of L-malate from 833 to 1263 cm^{-1} is scarce, correctness cannot be confirmed, although Kumar et. al. found an absorbance peak at around 1100 cm^{-1} that shows overlap with the peak from 1000 to 1100 cm^{-1} to some degree.

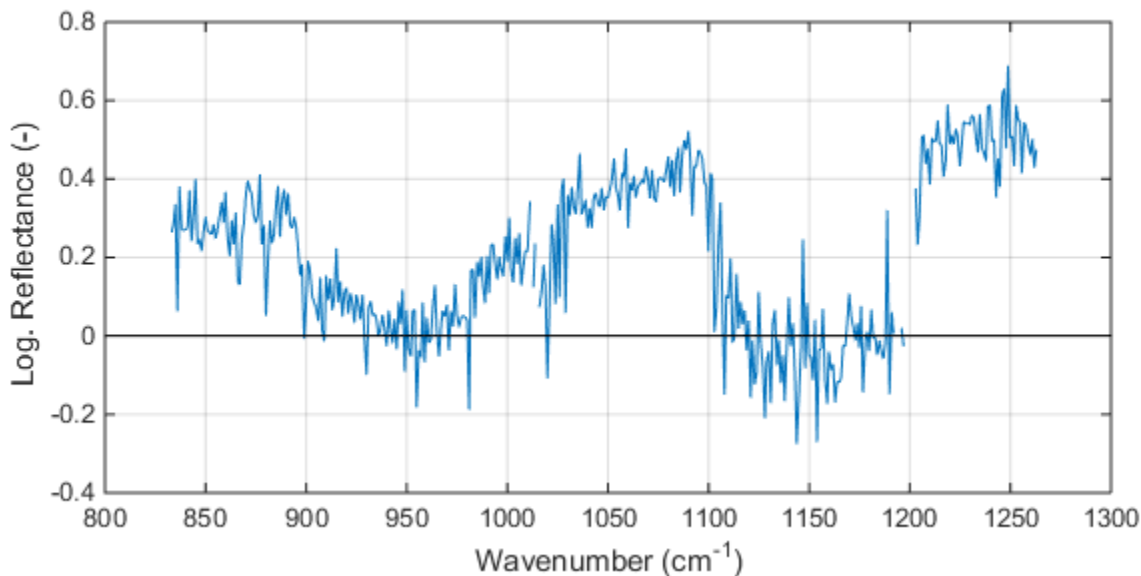


Figure 4.6 – Spectrum of 100 mM L-malate in buffer at room temperature.

The dehydration of malate into fumarate, catalysed by fumarase, was recorded for three different concentrations. For 10 mM and 20 mM malate the FLIR A655sc camera was used and for 100 mM the FLIR A6753sc was used. Figure 4.7 shows the course of the temperature difference following equation 4.2. Exponential decay of the temperature is observed, described by Newton's law of cooling. This law states the rate of temperature change $\frac{\delta T}{\delta t}$ is proportional to the temperature difference between the enzymes and the L-malate solution ($T - T_{Enz}$), resulting in a first-order differential equation. Solving this differential equation yields the exponential decay. It's important that all liquids are at the same temperature, but even if this were the case an exponential decay would still be observed, since in practice it's nearly impossible to get the tip of the pipette at the same temperature. For this reason a horizontal and vertical black line is shown in figure 4.7. The horizontal line indicates the average temperature before the addition of enzymes and the vertical line indicates the time corresponding to the first frame where the pipette is out of the ROI and the enzymes are added.

Three experiments were performed in relation to the dehydration of L-malate. In short, the experiments were the addition of 10 μL 15 mg/mL fumarase to 300 μL 10 mM L-malate, the addition of 20 μL 15 mg/mL fumarase to 290 μL 20 mM L-malate and the addition of 20 μL 15 mg/mL fumarase to 300 μL 100 mM L-malate. Only the results of the last experiment suggested the observation of temperature rise due to the reaction, see figure 4.8. From 50 to 70 seconds a clear

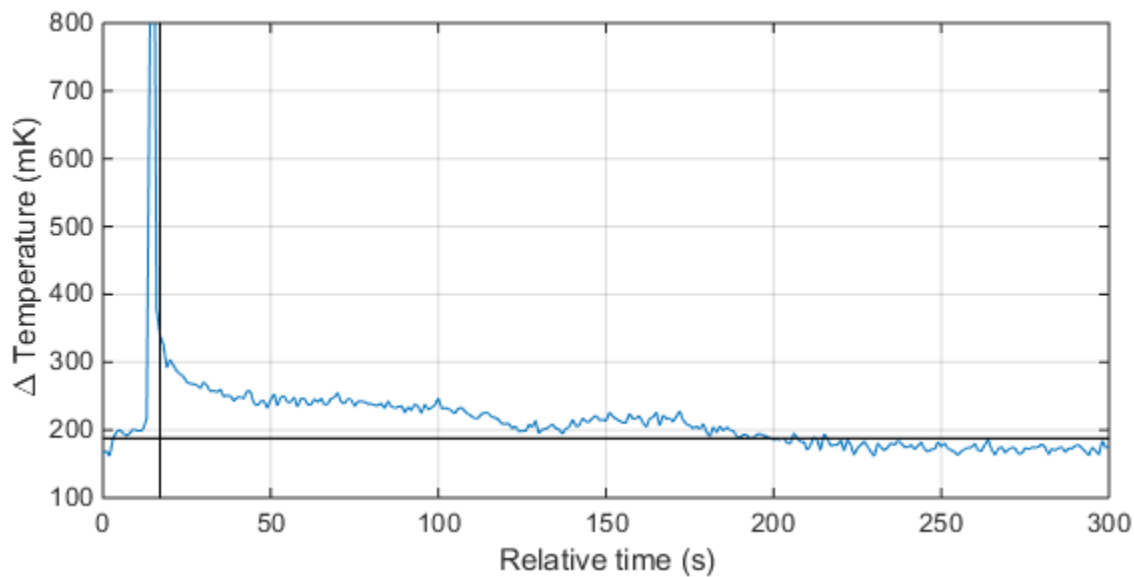


Figure 4.7 – 20 μ L of 15 mg/mL fumarase is added to 290 μ L 20 mM L-malate in buffer. The massive peak of over 800 mK is caused by the relatively high temperature of the tip of the pipette.

increase is shown. After thorough observation of the clip no external factors were found to play a role in this rise, making it more likely to be a result of the dehydration. However, the dehydration of L-malate is endothermic so a drop was expected rather than an increase. After repeating the experiment a similar, though less clear, temperature rise was observed, see figure C.8 in appendix C. These results are hard to interpret, because the pipetting is dominant. All other test results for the dehydration of L-malate can also be found in appendix C.

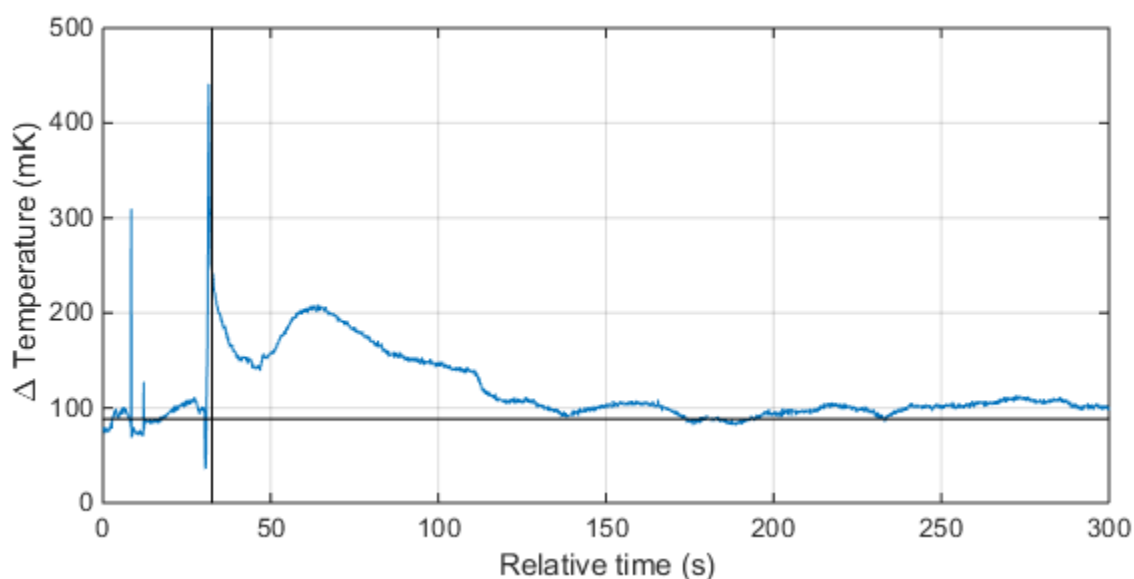


Figure 4.8 – 20 μ L of 15 mg/mL fumarase is added to 300 μ L 100 mM L-malate.

4.5 Thermal imaging of the oxidation of DAB and L-tyrosine

For the oxidation of DAB and Tyr only thermal imaging was performed, since it is only used for testing the camera's performance, in this case the FLIR A6753sc. Figure 4.9 shows the temperature difference for oxidation of 20 μL 10 mM DAB to 300 μL buffer. No features are observed that suggest the sensing of temperature differences due to the exothermic reaction. An explanation could be that the reaction does not produce enough heat to create distinguishable effects. Another explanation could be that the reaction happens too quickly and is not visible against the steep slope of the exponential decay. The same holds for the oxidation of L-tyrosine. All thermal data is presented in appendix C.

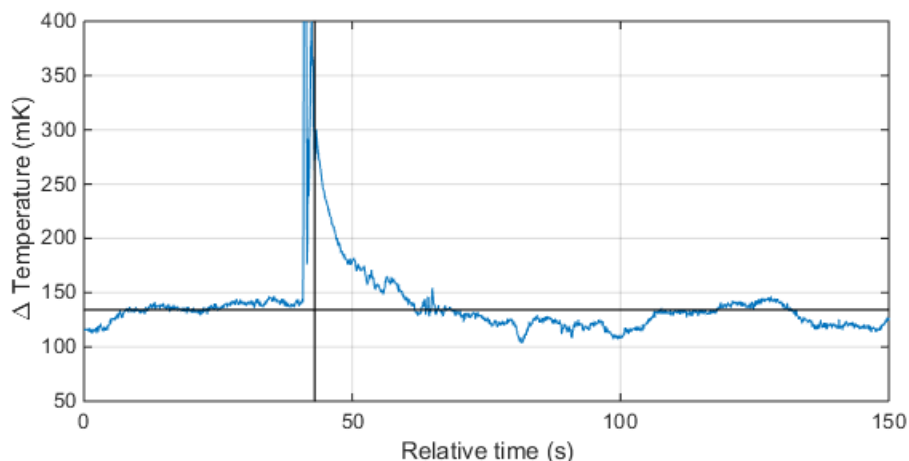


Figure 4.9 – Addition of 2 μL 2 mg/mL soybean peroxidase to a solution containing 300 μL buffer and 20 μL 10 mM DAB and 20 μL 5 mM hydrogen peroxide.

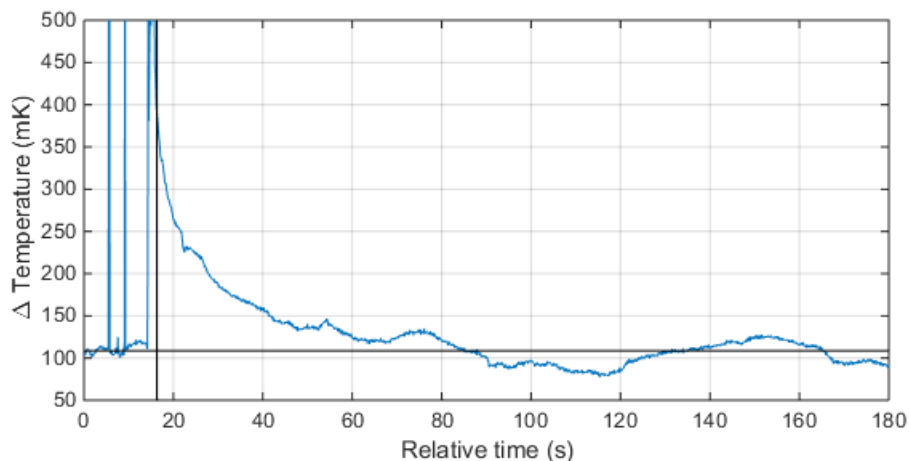


Figure 4.10 – Addition of 20 μL 2 mg/mL soybean peroxidase to a solution of 300 μL 2.50 mM Tyr and 20 μL 150 mM hydrogen peroxide.

5. Conclusion and outlook

In this project the goal was to design and construct a new experimental setup for observing enzymes in action. For this the setup had to perform specular reflectance spectroscopy and thermal imaging on enzyme catalyzed reactions simultaneously. Specular reflectance spectroscopy allows for detection and determination of the reactants, while thermal imaging provides information on temperature differences. Currently temperature differences due to enzyme catalyzed reactions are being monitored using calorimetry, an intrinsically slow method of measuring heat generation that requires independent validation on the products that are formed. As an alternative thermal imaging in combination with specular reflectance spectroscopy can be used to monitor an enzyme catalyzed reaction with reduced interfering by instruments, therefore limiting artefacts in the data.

It was intended that specular reflectance spectroscopy was performed with a QCL. For this the acquisition of voltages of the MCT detectors was tested and improved. It was observed that the detector voltage is directly proportional to the beam intensity. A first version of the spectroscopic setup was built and showed major differences between the internal and external detector, mainly a result of beam displacement. Performing a scan with this first version required six subscans, each covering a small part of the complete QCL spectrum. The spectrum of ethanol was recorded in 15 minutes in total, and showed a broad peak around 1060 cm^{-1} , in good agreement with ethanol's known spectrum. Improvements were made on the setup by altering the way the beam is focussed onto the external detector. Using this improved setup the ethanol spectrum was recorded and the spectrum showed agreement for $833\text{ to }1180\text{ cm}^{-1}$, an improvement in comparison with initial results.

Spectroscopy on L-malate showed a peak near 1100 cm^{-1} . The dehydration of L-malate, catalyzed by fumarase, was monitored using a FLIR camera. A microtiter plate containing the reactants was recorded for a certain period of time by the camera, while the enzyme (fumarase) was added during the recording. Plotting the temperature difference showed an exponential decay, most likely a consequence of Newton's law of cooling. For 100 mM L-malate an unexpected increase was observed twenty seconds after addition of the enzyme. The oxidation of DAB and tyrosine was recorded as well, although spectroscopy was not performed for these reactions. No features were recorded that could indicate temperature changes as a result of the oxidations.

The FLIR cameras that were used both showed noise in the order of tens of millikelvin, following their datasheet. This suggests that temperature differences of the same order might be possible to detect. However, controlling environmental factors proved to be most challenging, as temperature changes in the order of 100 millikelvin is common in laboratories. Another challenge is controlling the temperature of the added enzyme. By adding an enzyme solution at exactly the same temperature as the substrate solution the exponential decay may be reduced.

For future research the scanning time of the QCL using the LabVIEW VI needs to be reduced to

less than ten seconds. This will allow recording spectroscopic data every ten seconds, therefore measuring the concentration of reactants at higher temporal resolution. However, it is more important to improve the thermal imaging of reactions. Temperature stabilisation of the solutions can be achieved by placing the microtiter plate in an insulated styrofoam box. Additionally a different method of starting the reaction to increase repeatability and reliability has to be followed. One suggestion is to add the substrate during the recording in all wells simultaneously, minutes after the addition of the enzyme. This should drastically decrease the role of the exponential decay in recording the temperature difference, since all wells should follow roughly the same decay. Combining all these measures should allow for performing specular reflectance spectroscopy and thermal imaging simultaneously. This combination could provide a new method of screening enzyme assays.

Bibliography

- [1] A. Reyes-Reyes, Z. Hou, E. van Mastrigt, R.C.Horste, J.C. de Jongste, M.W. Pijnenburg, H.P. Urbach, and N. Bhattacharya. *Multicomponent gas analysis using broadband quantum cascade laser spectroscopy*, volume 22. Optical Society of America, 2014.
- [2] Zhe Hou. Breath analysis using infrared spectroscopy. Master's thesis, Delft University of Technology, 2013.
- [3] Olav Grouwstra. Breath analysis by quantum cascade laser spectroscopy. Master's thesis, Delft University of Technology, 2015.
- [4] <http://www.flir.eu/surveillance/content/?id=63482>. Accessed: 2015-02-24.
- [5] <http://energy.gov/energysaver/thermographic-inspections>. Accessed: 2015-02-24.
- [6] Irma Jrvel, Suvi Torniainen, and Kaija-Leena Kolho. *Molecular genetics of human lactase deficiencies*, volume 41. 2009.
- [7] B.P. Abbott et. al. *Observation of Gravitational Waves from a Binary Black Hole Merger*, volume 116. American Physical Society, Feb 2016.
- [8] Terence H. Risby and Frank K. Tittel. *Current status of midinfrared quantum and interband cascade lasers for clinical breath analysis*, volume 49. 2010.
- [9] Block Engineering. *LaserScope User Manual*.
- [10] P. A. M. Dirac. *On the Theory of Quantum Mechanics*, volume 112. The Royal Society, 1926.
- [11] S.O. Kasap. *Optoelectronics and Photonics*. Pearson, second edition, 2013.
- [12] <http://www.physik.hu-berlin.de/en/fet/research/light-emitters-based-on-intersubband-transitions-quantum-cascade-laser-physics-1>. Accessed: 2015-03-03.
- [13] Siyuan Yu, Jean-Michel Lourtioz, and Richard de la Rue. *Compact Semiconductor Lasers*. Wiley, 2014.
- [14] Jerome Faist, Federico Capasso, Deborah L Sivco, Carlo Sirtori, Albert L Hutchinson, and Alfred Y Cho. *Quantum cascade laser*, volume 264. American Association for the Advancement of Science, 1994.
- [15] Richard Maulini, Mattias Beck, Jérôme Faist, and Emilio Gini. *Broadband tuning of external cavity bound-to-continuum quantum-cascade lasers*, volume 84. AIP Publishing, 2004.

- [16] https://upload.wikimedia.org/wikipedia/commons/thumb/5/5b/Blazed_grating.svg/2000px-Blazed_grating.svg.png. Accessed: 2015-03-04.
- [17] G. L. Hansen, J. L. Schmit, and T. N. Casselman. *Energy gap versus alloy composition and temperature in $Hg_{1-x}Cd_xTe$* , volume 53. 1982.
- [18] National Instruments. *24-Bit Flexible-Resolution Digitizers: NI 5922*.
- [19] VIGO System S.A. *PVI4-TE Series*.
- [20] J.M. Chalmers, H.G.M. Edwards, and M.D. Hargreaves. *Infrared and Raman Spectroscopy in Forensic Science*. John Wiley, 2012.
- [21] J.D.E. McIntyre and D.E. Aspnes. *Differential reflection spectroscopy of very thin surface films*. North-Holland Publishing Co., 1970.
- [22] A. Kocak, S. L. Berets, V. Milosevic, and M. Milosevic. *Using the Kramers–Kronig Method to Determine Optical Constants and Evaluating Its Suitability as a Linear Transform for Near-Normal Front-Surface Reflectance Spectra*, volume 60. OSA, Sep 2006.
- [23] http://www.satoriseal.com/technical/technical_articles/compound_identification_in_quality_control.htm. Accessed: 2015-04-30.
- [24] Vincent Docter. Spectroscopic measurements using a quantum cascade laser. Master’s thesis, Delft University of Technology, 2013.
- [25] http://www.thorlabs.com/newgrouppage9.cfm?objectgroup_id=903. Accessed: 2015-04-22.
- [26] Saroj Kumar and Andreas Barth. *Following enzyme activity with infrared spectroscopy*, volume 10. Molecular Diversity Preservation International, 2010.
- [27] Kenneth A. Johnson and Roger S. Goody. *The Original Michaelis Constant: Translation of the 1913 MichaelisMenten Paper*, volume 50. 2011. PMID: 21888353.
- [28] Malcolm Dixon and Edwin C. Webb. *Enzymes*. Academic Press Inc., third edition, 1979.
- [29] <https://www.ncjrs.gov/App/Publications/abstract.aspx?ID=138909>. Accessed: 2015-05-27.
- [30] Maria F. Falangola, Sang-Pil Lee, Ralph A Nixon, Karen Duff, and Joseph A Helpert. *Histological co-localization of iron in A β plaques of PS/APP transgenic mice*, volume 30. Springer, 2005.
- [31] FLIR. *FLIR A655sc*.
- [32] FLIR. *FLIR A6750sc*.
- [33] A. Reyes-Reyes. *Quantum Cascade Laser Spectroscopy*. PhD thesis, Delft University of Technology, 2016. In progress.

Appendices

A Project description

bioDATE MSc project proposal

Researcher #1 Name: Nandini Bhattacharya E-mail: N.Bhattacharya@tudelft.nl Department/Faculty: OP/ImPhys Expertise for the Project: IR spectroscopy	Researcher #2 Name: Peter-Leon Hagedoorn E-mail: P.L.Hagedoorn@tudelft.nl Department/Faculty: BT/TNW Expertise for the Project: Biochemistry and enzymology, Enzyme calorimetry
--	--

TITLE: Advanced IR imaging to monitor enzymes in action

SUMMARY: This project will be aimed for IR hyper-spectral imaging of chemical reactions where enzymes are the catalysing agents. The dynamics of heat production and consumption on the sample can be spectrally imaged for a surface area using quantum cascade laser.

Background

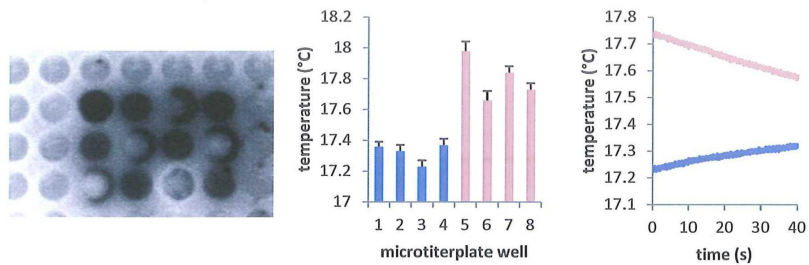
Enzymes are superior catalysts able to increase the rate of chemical reactions enormously with high specificity and under mild conditions. In order to use enzymes in the chemical industry it is necessary to engineer enzymes to have improved properties for a particular process. Systematic enzyme engineering approaches are available, however the development of enzyme activity screening assays is a bottleneck. There is a great desire to develop generic enzyme assays, that in principle, can be used to measure any enzyme with any substrate. The heat of a chemical reaction that can be measured using microcalorimetry is a direct measure of the rate of the (enzyme catalysed) reaction. Calorimetric techniques, however, are intrinsically slow hampering their use as a screening technique. Furthermore, calorimetry is a 'blind' technique that still requires independent validation of the products that are formed. Here we plan to study enzymes in specific chemical reactions by measuring the heat generated in the reactions in a different way.

Aim

To explore the possibility of IR imaging to image chemical reactions catalysed by enzymes both by measuring heat evolution or consumption and IR spectroscopy of substrate to product conversion simultaneously.

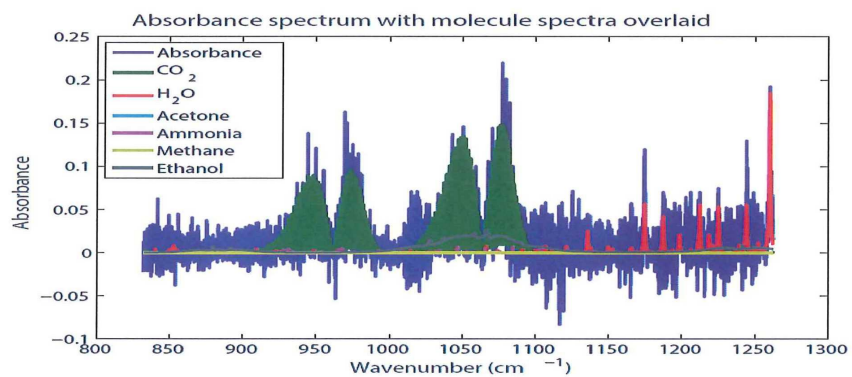
Approach

The student (TN with interest in chemistry, or MST/LST with ample matlab experience) will study the sample with the active chemical reaction by illuminating with a beam of IR laser radiation and imaged with a thermal imager. The illuminating beam will be scanned in the wavelength range of (850 – 1250 cm^{-1}) in 5.3s initially to determine the spectral range and the region of interest in the sample where maximum chemical activity is generated leading to the production of heat. The active regions can then be studied in detail at specific wavelengths [1].



IR thermographic imaging of catalase activity. The measurement solution consisted of 300 μ l 88 mM hydrogen peroxide in 50 mM KPi pH 7.0. The reaction was started by adding 0.07 mg/ml catalase. a) Thermographic image of the microtiter plate, b) average temperature in individual wells, c) time trace of the average temperature in an enzyme and non-enzyme containing well. The camera that was used is the FLIR SC7500 with an InSb detector. The camera records 320 \times 256 pixels, with a 1.5 \times 5.1 μ m spectral bandwidth and a 15 mK sensitivity.

The IR thermal imager will be used to measure the temperature change due to the heat evolved or consumed during the enzyme reaction. By combining the IR laser it will be possible to obtain molecular information using IR spectroscopy. Imaging will, in principle, allow the measurement of a large number of samples simultaneously.



References

1. Reyes-Reyes, A., Hou, Z., van Mastrigt, E., Horsten, R. C., de Jongste, J. C., Pijnenburg, M. W., Urbach, H. P. & Bhattacharya, N. (2014) Multicomponent gas analysis using broadband quantum cascade laser spectroscopy *Opt Express*. **22**, 18299-18309.

B Ethanol spectra for different concentrations

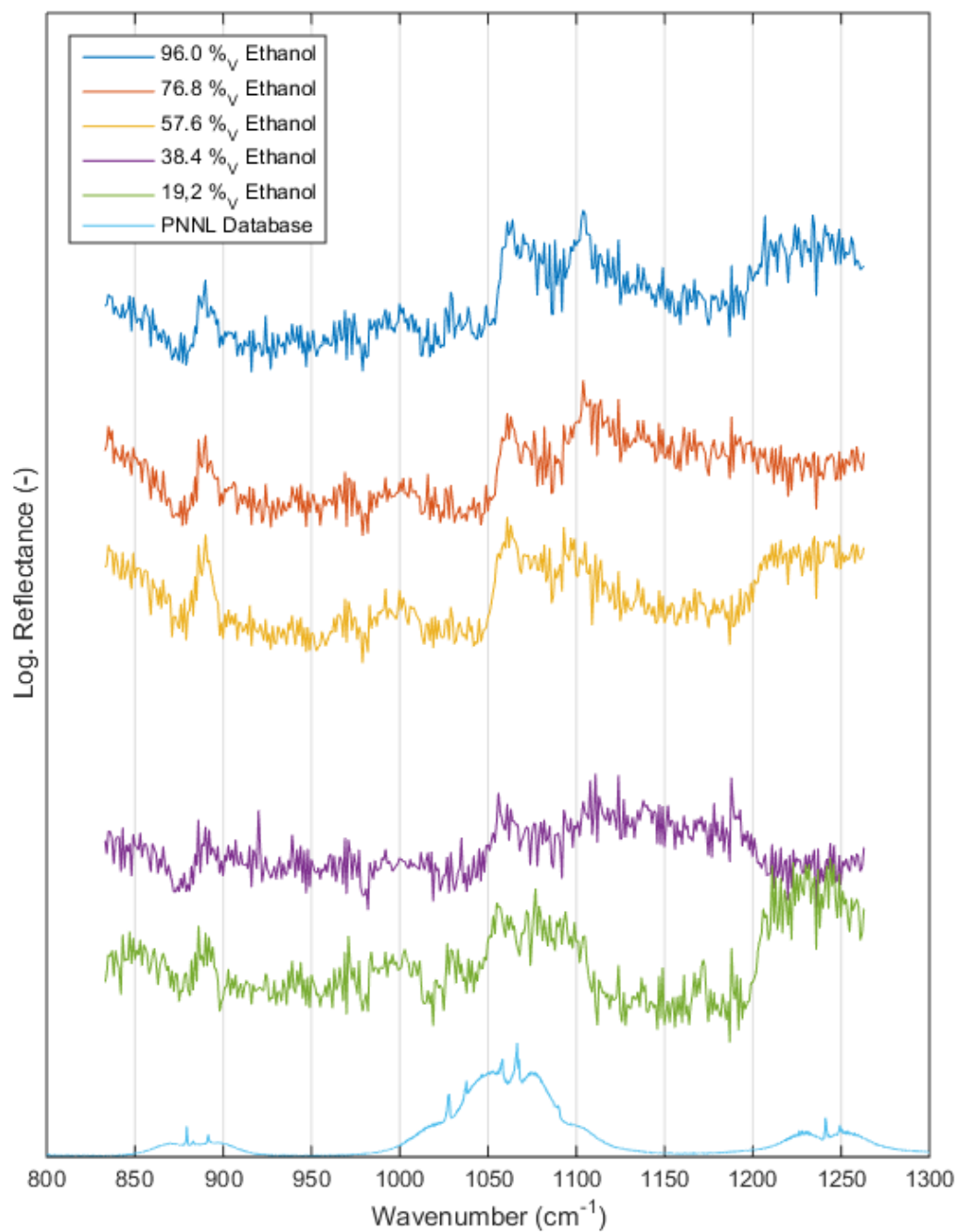


Figure B.1 – The ethanol spectrum for different concentrations. All graphs (except the 'PNNL Database') are elevated for easier mutual comparing.

C Thermal recordings of enzymatic reactions

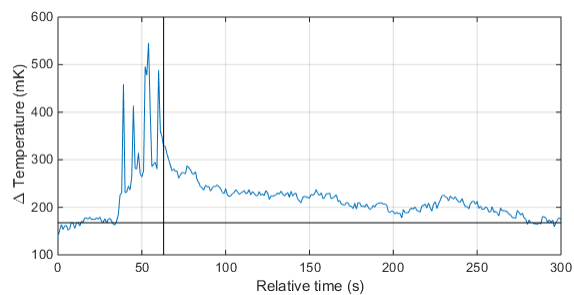


Figure C.1 – 10 mM L-malate.

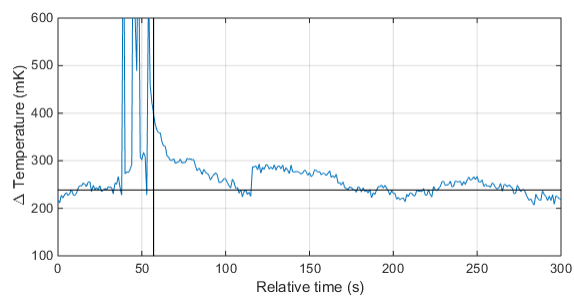


Figure C.2 – 10 mM L-malate.

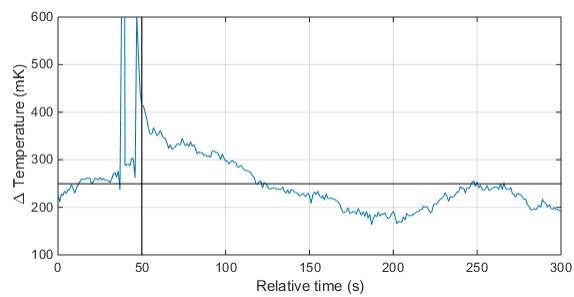


Figure C.3 – 10 mM L-malate.

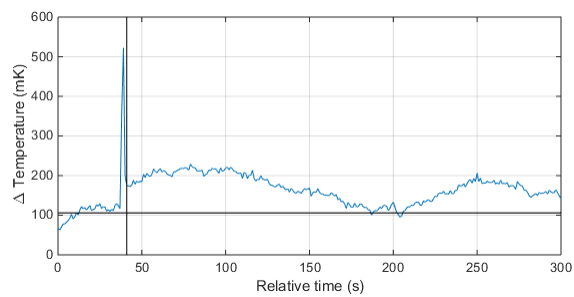


Figure C.4 – 10 mM L-malate.

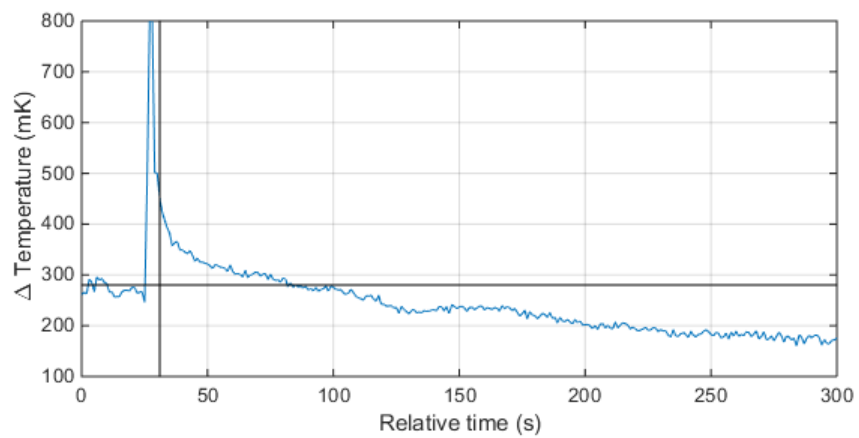


Figure C.5 – 20 mM L-malate.

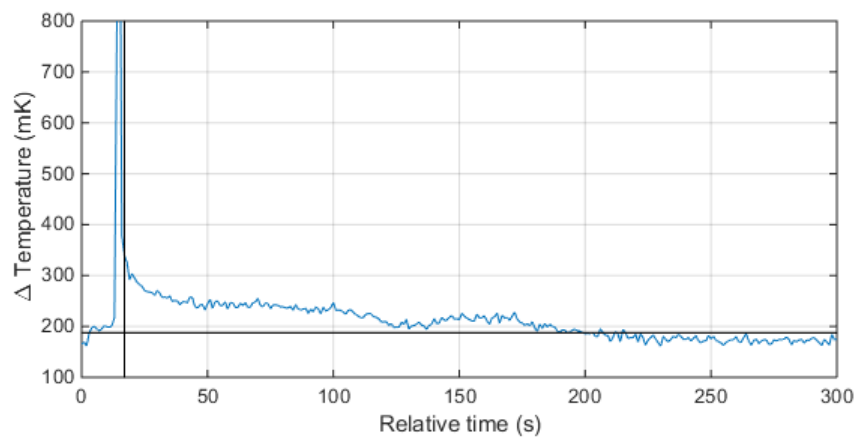


Figure C.6 – 20 mM L-malate.

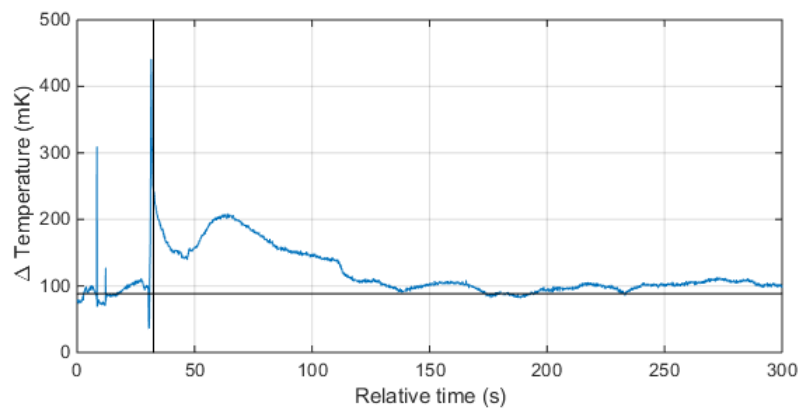


Figure C.7 – 100 mM L-malate.

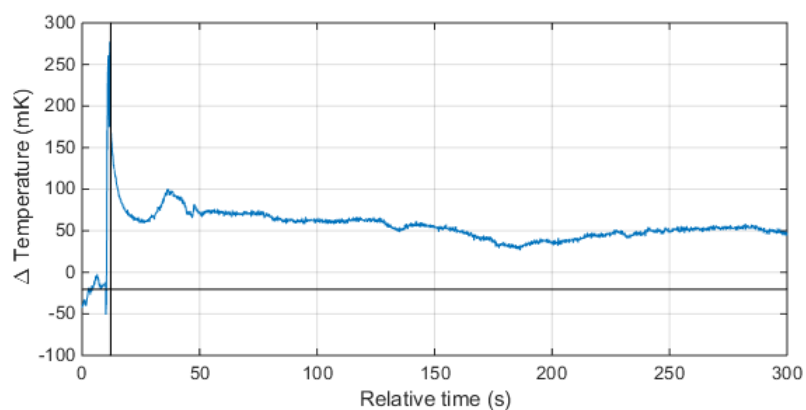


Figure C.8 – 100 mM L-malate.

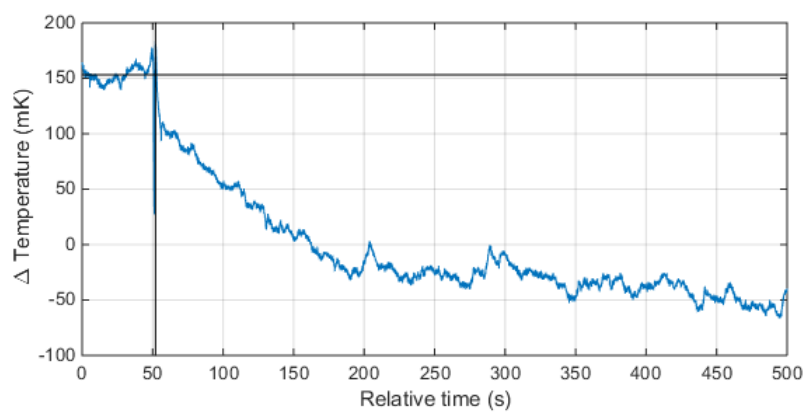


Figure C.9 – 100 mM Malate.

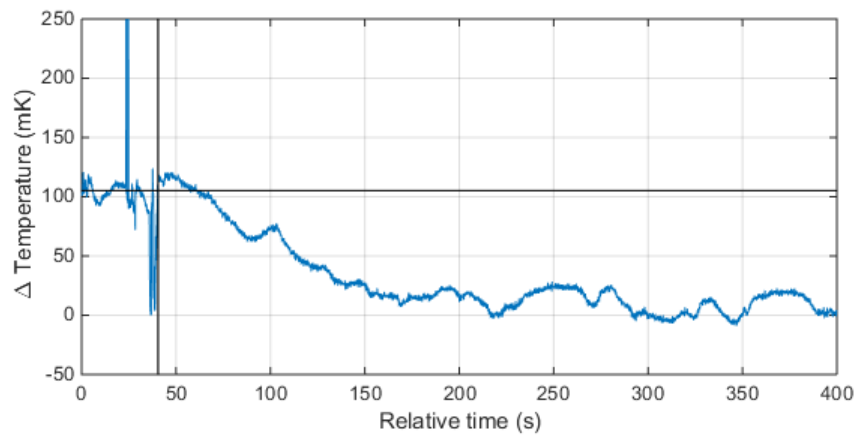


Figure C.10 – 6.5 mM DAB.

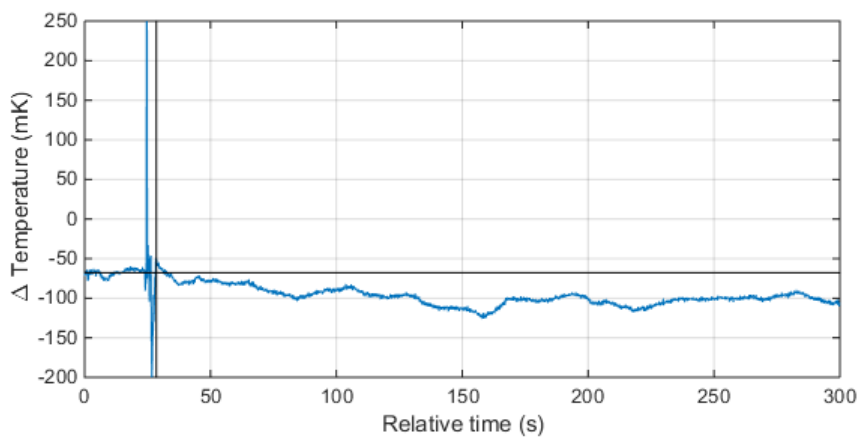


Figure C.11 – 6.5 mM DAB.

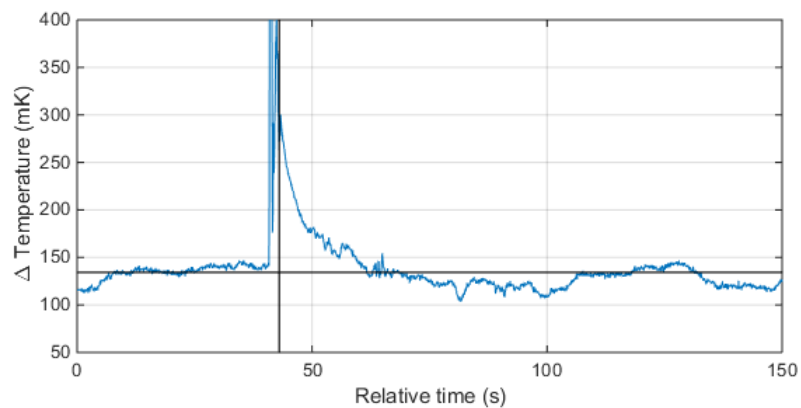


Figure C.12 – 10 mM DAB.

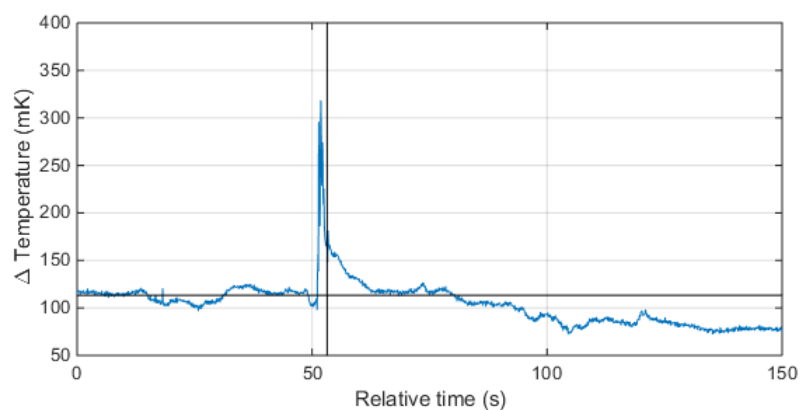


Figure C.13 – 10 mM DAB.

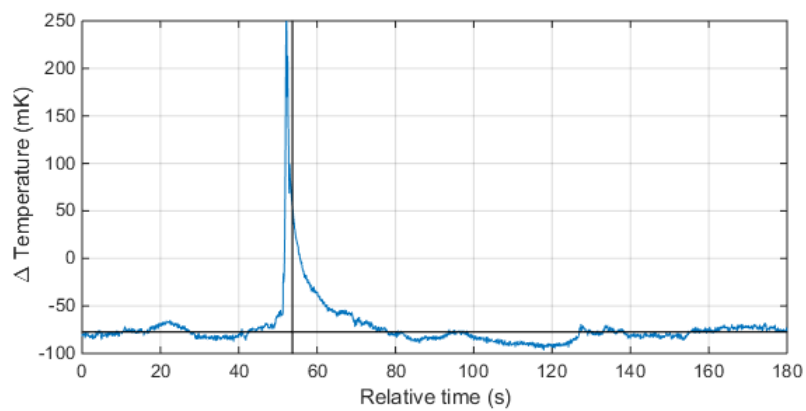


Figure C.14 – 10 mM DAB.

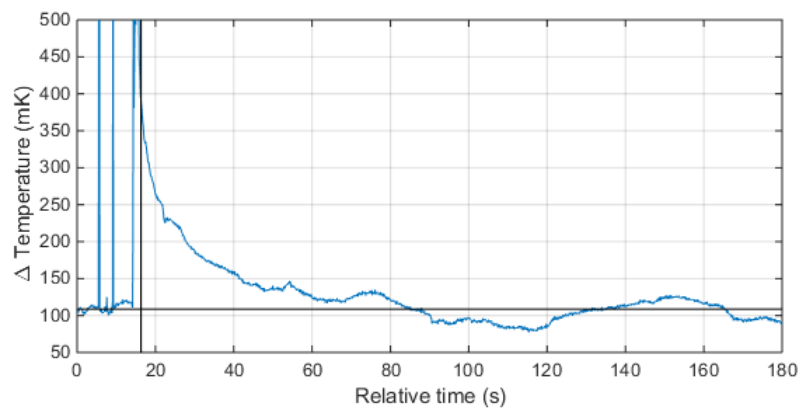


Figure C.15 – 2.5 mM tyrosine.

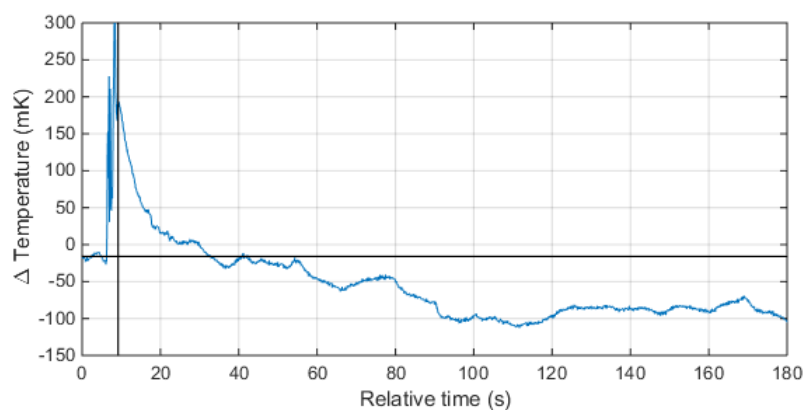


Figure C.16 – 2.5 mM tyrosine.

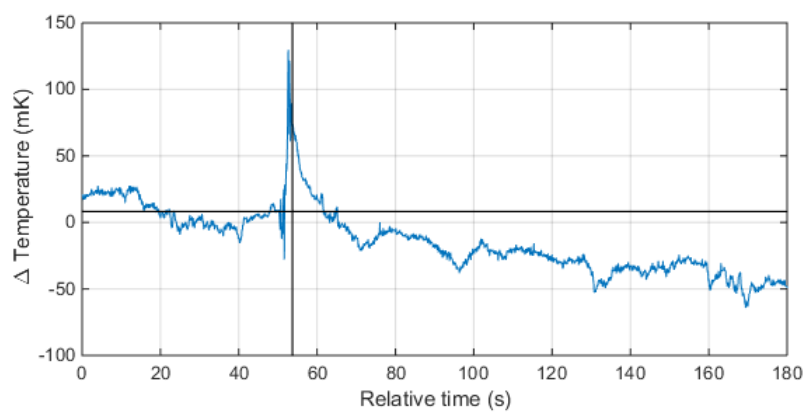


Figure C.17 – 2.5 mM tyrosine.

Acknowledgement

Als eerste wil ik mijn dank uitspreken aan de opleiding Technische Natuurkunde voor vier gezellige, leerzame en fantastische jaren. Uiteraard kan ik de opleiding niet in haar volledigheid bedanken zonder de studievereniging Ångström uit te lichten. Bedankt voor de vele uurtjes vermaak die jullie vele studenten hebben bezorgd.

Mijn dank gaat uit naar Nandini Bhattacharya, Yvonne van Aalst, Roland Horsten en Thim Zuidwijk voor hun support en hun wil om te helpen. Ook wil ik Peter-Leon Hagedoorn bedanken voor zijn input in dit project en zijn bereidheid om moeilijkheden en data te bespreken. Bovendien wil ik Koen Jacobs van FLIR bedanken voor zijn gastvrijheid, mening en bereidheid om twee cameras aan ons uit te lenen.

Als laatste gaat uiteraard mijn dank uit naar mijn ouders en mijn zus voor hun liefde en behulpzaamheid in de drukke, stressvolle en minder vrolijke dagen de afgelopen tijd. Bedankt voor alle steun.